University of Reading

Surging of global surface temperature due to decadal legacy of ocean heat uptake

Article

Accepted Version

It is advisable to refer to the publisher's version if you intend to cite from the work. See Guidance on citing.

www.reading.ac.uk/centaur

CentAUR

1 **Surging of global surface temperature due to decadal legacy of ocean heat uptake**

2 Bablu Sinha[1], Florian Sévellec[2,3], Jon Robson[4] and George Nurser[1]

3

4 [1]National Oceanography Centre, UK

5 [2]Laboratoire d'Océanographie Physique et Spatiale, Univ Brest CNRS IRD Ifremer,

6 Brest, France

7 [3]Ocean and Earth science, University of Southampton, Southampton, UK,

8 [4]National Centre for Atmospheric Science, Dept of Meteorology, University of

9 Reading, UK

10

11 Corresponding Author: Bablu Sinha, email bs@noc.ac.uk

12

13

14   **Abstract**

15   Global surface warming since 1850 consisted of a series of slowdowns (hiatus)

16   followed by surges. Knowledge of a mechanism to explain how this occurs would aid

17   development and testing of interannual to decadal climate forecasts. In this paper a global

18   climate model is forced to adopt an ocean state corresponding to a hiatus (with negative

19   Interdecadal Pacific Oscillation, IPO, and other surface features typical of a hiatus) by

20   artificially increasing the background diffusivity for a decade before restoring it to its normal

21   value and allowing the model to evolve freely. This causes the model to develop a decadal

22   surge which overshoots equilibrium (resulting in a positive IPO state) leaving behind a

23   modified, warmer climate for decades. Water mass transformation diagnostics indicate that

24   the heat budget of the tropical Pacific is a balance between large opposite signed terms:

25   surface heating/cooling due to air-sea heat flux is balanced by vertical mixing and ocean heat

26   transport divergence. During the artificial hiatus, excess heat becomes trapped just above the

27   thermocline and there is a weak vertical thermal gradient (due to the high artificial

28   background mixing). When the hiatus is terminated, by returning the background diffusivity

29   to normal, the thermal gradient strengthens to pre-hiatus values so that the mixing (diffusivity

30   x thermal gradient) remains roughly constant. However, since the base layer just above the

31   thermocline remains anomalously warm this implies a warming of the entire water column

32   above the trapped heat which results in a surge followed by a prolonged period of elevated

33   surface temperatures.

34

1. Introduction

The estimated 0.85K global surface warming since 1850 (IPCC, 2013) was realized as a succession of periods of stronger followed by weaker warming (Risbey 2015). Understanding the causes of these hiatus and surge events is of key importance for interannual-to-decadal prediction (Guemas et al. 2013; Meehl et al. 2014; Sévellec and Drijfhout 2018) and for constraining uncertainty in long-term climate projections.

A large uncertainty remains concerning the detailed processes responsible for surge and hiatus periods, with debate centered around the relative roles of external forcing (anthropogenic greenhouse gas and aerosol emission variations, solar radiation changes, volcanic eruptions) versus internal variability (Smith et al. 2015) and the dominance or otherwise of the Pacific over the Atlantic (England et al. 2014; Chen and Tung 2014; Drijfhout et al. 2014; Meehl et al. 2011).

During the recent global surface warming hiatus of the 2000s Smith et al. (2015) estimated a reduction in net top-of-atmosphere (TOA) radiation of -0.31 ± 0.21 W m^{-2} between 1999 and 2005, but could not identify whether this was due to internal processes or external drivers. Even if the source of the TOA reduction were disentangled, Song et al. (2014) demonstrate using the CMIP5 multimodel ensemble that on decadal timescales TOA imbalance is only very weakly related to surface air temperature (SAT), because natural variability is superimposed on global warming (see also Xie et al. 2016). Also, Hedemann et al. (2017) point out that it is the difference between TOA imbalance and ocean heat transfer between the surface (~100 m) layer and the deep ocean which matters for a hiatus, and this could be too small (~0.08 W m^{-2}) to resolve, with the current observing system.

59   Leaving aside the ultimate causes of hiatus and surge events (external forcing versus internal

60   variability), the hiatus of the 2000s coincided with a negative phase of the Interdecadal

61   Pacific Oscillation (IPO) consistent with the results of Meehl et al (2013) who found the IPO

62   as one of three main processes responsible for hiatus and surge behaviour in the CCSM4

63   coupled climate model, the others being Antarctic Bottom Water Formation and the Atlantic

64   Meridional Overturning Circulation (AMOC). Observations demonstrated that the hiatus was

65   associated with anomalously cold Pacific sea-surface temperatures (SSTs) and warm

66   thermocline anomalies (Nieves et al. 2015), due to strengthened subtropical circulation cells

67   forced by strengthened trade winds (Farneti et al. 2014; England et al. 2014).   That the IPO,

68   especially the equatorial Pacific, played a key role in the hiatus was demonstrated by England

69   et al. (2014), Watanabe et al. (2014), and Kosaka and Xie (2014) using pacemaker

70   experiments where either Tropical Pacific winds or SST were forced to follow observations in

71   coupled model simulations, which then reproduced the hiatus. However increased ocean heat

72   uptake was also seen in the deep North Atlantic and Southern Oceans during this period

73   (Balmaseda et al. 2011; Chen and Tung 2014; Drijfhout et al. 2014) and the role of these

74   regions, especially the North Atlantic where the AMOC is strongly associated with heat

75   content changes (Moat et al., 2018; Willliams et al. 2015) and the Surface Atmospheric

76   Temperature (SAT) is highly variable (Sévellec et al. 2016), remains unclear.

77   More recent work has documented the long residence time of heat taken up by the

78   ocean and stored below the mixed layer during the recent hiatus of the 2000s. Maher et al.

79   (2018), using an ocean model forced by negative IPO-like surface atmospheric conditions,

80   found drawdown of heat into the main thermocline (~300-m depth) and surface cooling in the

81   Pacific. The extra subsurface heat was advected by subtropical cells, strengthened as a result

82   of enhanced trade winds, into the Indian Ocean where it remained buried in the thermocline,

83   as seen earlier in analysis of hiatus periods in the CMIP5 multimodel ensemble (Lee et al.

84   2015). A similar result was found in the pacemaker experiments of Gastineau et al. (2019),

85   although the spatial redistribution of heat showed differences, for example much of the

86   additional heat entering the Indian Ocean from the Pacific during the hiatus was returned to

87   the atmosphere via surface fluxes, or advected southwards into the Southern Ocean. The

88   spreading of this additional heat from the Pacific to the Indian Ocean, seen in observations as

89   well as models (Nieves et al. 2015; Liu et al. 2016; Lee et al., 2015) and its partial

90   reemergence after the hiatus suggests a substantial legacy of, and potentially an active role

91   for, the ocean heat uptake during the hiatus period. This was illustrated in the Maher et al.

92   (2018) study by the response to a subsequent reversal of IPO phase, in which the sequestered

93   heat was not re-extracted back to the atmosphere.

94   The consensus then, is that the IPO determines the pattern of heat drawdown above

95   the tropical thermocline and subsequent horizontal redistribution via associated changes in the

96   strength of the shallow subtropical overturning cells.

97   The significance of the increased heat uptake seen in the deep Southern and North Atlantic

98   Oceans (Meehl et al. 2013; Drijfhout et al. 2014; Chen and Tung, 2014) remains ambiguous.

99   Indeed, Drijfhout et al. (2014) suggest that the enhanced Southern Ocean heat uptake may be

100 an ongoing multidecadal process linked to external forcing of the Southern Annular Mode

101 rather than natural variability. The role of the North Atlantic remains a thorny issue with the

102 mechanism relating AMOC changes to ocean heat uptake still debated (Chen and Tung, 2014

103 versus Drijfhout et al. 2014).

104   The central role of ocean heat uptake in variations of global mean surface temperature

105 and the TOA radiation balance motivates us to explore the effects of its variability on decadal

106 timescales. Tanaka et al. (2012) show that changes in ocean mixing can affect Pacific decadal

107 variability, a key player in the hiatus of the early 2000s (Meehl et al. 2011; England et al.

108 2014; and others, see above). Hence here we explore the effects of transient enhancement of

109   ocean mixing, and the subsequent climate adjustment, on ocean heat uptake and global mean

110   surface temperature.

111

112   **2. Method**

113

114   **2.1 Climate model and experiment design**

115

116   We use the HadCM3 climate model (Gordon et al. 2000 which maintains a stable

117   climate simulation without flux adjustments despite relatively coarse grid resolution (1.25° x

118   1.25° ocean/3.75° x 2.5° atmosphere).   The HadCM3 preindustrial control simulation

119   provides a reasonable simulation of the observed energy flows between components of the

120   Earth System (Table 1). We spin experiments off the control by instantaneously doubling the

121   background vertical diffusivity at every gridpoint and integrating the model for one decade

122   before instantaneously returning the diffusivity to its control value and continuing the

123   integration for one or more further decades. To address internal variability we create a 4-

124   member ensemble by starting from different points of a 140-year portion of the 2000-year

125   control simulation. All ensemble members begin on the same day of the year, December 1.

126

127   The *in situ* vertical diffusivity for tracers consists of a time-independent (background)

128   part, which only varies with depth and a time-dependent part which depends on the

129   stratification and velocity shear present and varies spatially and temporally (Gordon et al.

130   2000, Appendix 2). The background part increases with depth from $\sim10^{-5}$ m^2 s^{-1} at the surface

131   to $\sim15\times10^{-5}$ m^2 s^{-1} in the abyss (Gordon et al. 2000). We instantaneously double this

132   background part at the beginning of the ensemble experiment and set it back to normal at the

133   beginning of the second decade. Ocean models also include substantial numerical mixing up

134 to several times the explicit mixing (Megann 2018), hence the mixing perturbation we apply

135 only modifies the actual *in situ* mixing coefficient by perhaps 10-20%, not far removed from

136 its observational uncertainty.

137

138 Ensemble mean quantities are evaluated for significance against the control (all

139 variables are first filtered using a 5-year running mean unless otherwise stated) using a one

140 tailed *t*-test, taking into account the number, *n*, of independent degrees of freedom in the 140

141 year control simulation (estimated to be *n*=26 due to autocorrelation in the time series).

142

143 **2.2 Watermass transformation framework**

144

145 Since we modify the diffusion coefficient and hence the mixing in our experiments, a

146 natural framework for diagnosis of the results is water mass transformation analysis (Walin

147 1982). The strength of this framework is that it diagnoses mixing from all sources, including

148 numerical mixing, which cannot easily be quantified by alternative methods (Megann 2018;

149 Lee et al. 2002). Additionally, the water mass transformation framework can be applied

150 directly to observations and was developed in that context (Walin 1982).

151 For convenience of exposition, we describe this framework for a zonally integrated

152 domain, however the extension to three dimensions is important for the real ocean, hence we

153 also discuss how to interpret the equations in a 3D context.

154 Referring to Fig 1(a), we begin with the 'transformation' i.e. the rate $G(\theta, \phi)$ at which

155 water crosses some isotherm with potential temperature θ integrated zonally over all

156 longitudes, λ, and meridionally north of some latitude ϕ. This is related by mass (or volume

157 in a Boussinesq fluid) conservation to the meridional influx across ϕ,

158

159
$$\psi(\theta, \phi) = \iint_{\lambda, z: \theta'(\lambda, \phi, z) < \theta} v\,R \cos\phi\;dz d\lambda\,, \tag{1}$$

160   of water colder than θ (where v is meridional velocity, and R is the radius of the Earth)

161   and the rate of change of the volume $V(\theta, \phi)$ north of ϕ and colder than θ by

162
$$\frac{\partial V(\theta, \phi)}{\partial t} = \psi(\theta, \phi) - G(\theta, \phi) \tag{2}$$

163   This transformation $G(\theta, \phi)$ represents water crossing the isotherm from cool to

164   warm, and thus requires heat input; to link $G(\theta, \phi)$ to heat inputs we consider (Fig. 1b) the

165   (Boussinesq) equation for the heat content of water colder than θ (e.g. Nurser et al., 1999):

166
$$\frac{\partial \mathbb{H}}{\partial t} = -D_{\text{diff}} - D_{\text{surf}} + A - c_p \rho_0 G \theta. \tag{3}$$

167   Here

168
$$\mathbb{H} = \rho_0 c_p \iiint_{\lambda, \phi', z: \theta'(\lambda, \phi', z) < \theta, \phi' < \phi} \theta' R \cos\phi'\;d\lambda\,d\phi dz \tag{4}$$

169   is the heat contained within seawater with potential temperature less than or equal to θ

170   integrated everywhere north of a given latitude ϕ and $\frac{\partial \mathbb{H}}{\partial t}$ is its time derivative. D_{diff} is the

171   (cold-to-warm) diffusive temperature flux across the θ isotherm north of latitude ϕ due to

172   mixing, while

173
$$D_{\text{surf}} = -\iint_{\lambda, \phi: \theta_s(\lambda, \phi) \leq \theta} I(\lambda, \theta, z_\theta)\;R \cos\phi\;d\lambda\,d\phi$$

174
$$-\iint_{\lambda, \phi: \theta_s(\lambda, \phi) \leq \theta} (I_s - Q_{\text{net}}(\lambda, \phi))\;R \cos\phi\;d\lambda\,d\phi \tag{5}$$

175   represents the heat fluxes upwards and out (first term) through the θ isotherm due to solar

176   irradiance I (sign convention is +ve downwards) where the isotherm is close to the ocean

177   surface and upwards through the surface boundary where the θ isotherm has outcropped

178   (second term; the net turbulent air-sea flux $Q_{NET} = Q_{latent} + Q_{sensible} + Q_{LW}^{net}$ is made up of

179 (+ve upwards) latent, sensible and net longwave (LW) radiative heat fluxes and the surface

180 irradiance I_s is +ve downwards, note that, θ_s denotes the SST). The term

$$A(\theta, \phi) = \rho_0 c_p \iint_{\lambda,z:\theta'(\lambda,\phi,z)<\theta} \theta' v\, R \cos\phi\; dzd\lambda \qquad (6)$$

181

182 represents the advective heat transport of water colder than θ northwards across latitude ϕ,

183 while $c_p \rho_0 G\theta$ represents the advective heat flux up out across the θ isotherm.

184   Noting that the transport of water with $\theta < \theta' < \theta + \delta\theta$:

$$\delta\psi = \iint_{\lambda,z:\theta<\theta'(\lambda,\phi,z)<\theta+\delta\theta} v\, R \cos\phi\; dzd\lambda \approx \frac{\partial\psi}{\partial\theta}\cdot\delta\theta,$$

185

186 we can re-express (integrating by parts for the last result)

$$A(\theta, \phi) = \rho_0 c_p \int^{\theta} \frac{\partial\psi}{\partial\theta}\theta d\theta' = \rho_0 c_p \psi\theta - \rho_0 c_p \int^{\theta} \psi\, d\theta', \qquad (7a)$$

187

188 and similarly obtain:

$$\mathbb{H}(\theta, \phi) = \rho_0 c_p \int^{\theta} \frac{\partial V}{\partial\theta}\theta d\theta' = \rho_0 c_p V\theta - \rho_0 c_p \int^{\theta} V\, d\theta'. \qquad (7b)$$

189

190   Eliminating $\mathbb{H}$ and A from (3) using (7a) and (7b), and removing the $G\theta$, $\psi\theta$ and $\frac{\partial V}{\partial t}\theta$

191 terms using (2) gives

$$-\rho_0 c_p \int^{\theta} \frac{\partial V}{\partial t}d\theta' = -D_{\text{diff}} - D_{\text{surf}} - \rho_0 c_p \int^{\theta} \psi\, d\theta'.$$

192

193 Differentiating this by θ and again using (2) to replace $-\frac{\partial V}{\partial t} + \psi$ by G gives the key result

$$\rho_0 c_p G = -\frac{\partial D_{\text{diff}}}{\partial\theta} - \frac{\partial D_{\text{surf}}}{\partial\theta}\ . \qquad (8)$$

194

195   Multiplying (8) by $\delta\theta$ makes clear that (8) represents the heat budget of the volume

196 between the θ and $\theta + \delta\theta$ isotherms, relating the transformation (volume flux from cold to

197 warm) across the isothermal surfaces to the heat acquired from the convergence of air-sea

198 fluxes and mixing. It is customary to introduce F, the transformation driven by air-sea fluxesϕ

199
$$\rho_0 c_p F = -\frac{\partial D_{\text{surf}}}{\partial \theta};$$
(9)

200 it then follows (Fig. 1c) that

201 $\rho_0 c_p F \delta\theta = -\frac{\partial D_{\text{surf}}}{\partial \theta} \delta\theta$

202
$$= \iint_{\lambda,\phi:\phi'>\phi,\ \theta_s(\lambda,\phi)>\theta+\delta\theta} I(\lambda,\phi',z_{\theta+\delta\theta})\ \text{R}\cos\phi'\ d\lambda\ d\phi'$$

203
$$-\iint_{\lambda,\phi:\phi'>\phi,\ \theta_s(\lambda,\phi)>\theta} I(\lambda,\phi',z_\theta)\ \text{R}\cos\phi'\ d\lambda\ d\phi'$$

204
$$+\iint_{\lambda,\phi':\phi'>\phi,\theta<\theta_s(\lambda,\phi)\le\theta+\delta\theta} (I_s - Q_{\text{net}}(\lambda,\phi'))\ \text{R}\cos\phi\ d\lambda\ d\phi'$$
(10)

205 where the three terms on the RHS of (10) represent (i) the solar irradiation down through the

206 $\theta + \delta\theta$ isotherm (a heat source for the layer $\theta < \theta' < \theta + \delta\theta$) (ii) the solar irradiation down

207 through the θ isotherm (a heat sink) and (iii) the surface heat flux down through the outcrop

208 $\theta < \theta_s < \theta + \delta\theta$. In terms of F, the watermass transformation G is then given as

209
$$\rho_0 c_p G = \rho_0 c_p F - \frac{\partial D_{\text{diff}}}{\partial \theta}.$$
(11)

210 While it is in principle possible to evaluate the diffusive fluxes, they are difficult to evaluate

211 in observations and many models, so they are often in practice estimated as a residual

212 between G, (which can be found by (1) from changes in volume $\frac{\partial V}{\partial t}$ and transport ψ) and F

213 which is known from the surface fluxes.

214 We can use Eq (11) to eliminate G in Eq (2) arriving at

215
$$\frac{\partial V(\theta,\phi)}{\partial t} = \psi(\theta,\phi) - F(\theta,\phi) + \frac{1}{c_p\rho_0}\frac{\partial D_{\text{diff}}}{\partial \theta}$$
(12)

216 Now $\frac{\partial V}{\partial \theta}\delta\theta$ represents the volume of water with temperature between θ and $\theta + \delta\theta$,

217 so differentiating Eq (12) by θ gives:

218
$$\frac{\partial^2 V(\theta,\phi)}{\partial t\partial \theta} = \frac{\partial \psi(\theta,\phi)}{\partial \theta} - \frac{\partial F(\theta,\phi)}{\partial \theta} + \frac{1}{c_p\rho_0}\frac{\partial^2 D_{\text{diff}}}{\partial \theta^2}$$
(13)

10

219

220   which describes the increase in volume of water of temperature θ in terms of its southern

221   influx $\frac{\partial \psi(\theta,\phi)}{\partial \theta} \delta\theta$, and the convergence of flow across the θ and $\theta + \delta\theta$ isotherms.

222   To bring out the physical meaning in three dimensions of the terms in Eqs (12) and

223   (13), Fig. 1(d) shows simulated temperature in one particular December in a region of the

224   Pacific dominated by the shallow northern subtropical overturning cell (19.5°N-30°N, 140°E-

225   120°W and 0- 300m depth). The Equatorial warm pool is visible to the south west (θ>27°C).

226   From here, isotherms slope up, east- and northwards. Water between 22°C and 23°C (purple

227   shading outcrops at the surface in a crescent oriented northwest to south east. In 3D, the

228   watermass resembles a bowl shape truncated by the southern boundary of the region where

229   the watermass persists as a thin near-horizontal feature at about 80m depth at ,160°E

230   extending eastwards to about 160°W where it rises vertically to intersect the surface.

231   Applying Eq (12), we integrate the surface heat flux across all surface waters to the north with

232   23°C < θ ≤24°C (purple shaded surface region extending to the North Pole). This is the larger

233   yellow arrow ($F_{23°C, 19.5°N}$) , a loss of volume, which would be compensated in steady state by

234   flow of warmer water across the 23°C isotherm (solid black arrows). With the heat flux

235   integrated back to the North Pole, we cannot say anything about the latitudinal distribution of

236   this diapycnal flow. Now, restricting ourselves to waters to the north with 22°C < θ ≤23°C

237   we obtain a smaller value (smaller yellow arrow = $F_{22°C, 19.5°N}$) which must be balanced by a

238   diapycnal flow of water across the 22°C isotherm (dashed black arrows). Hence the

239   *difference*, i.e. applying Eq (13), between these two transformation rates (known as the

240   formation rate) results in a tendency for the volume of the purple region to increase.
241

242   The formation rate may be partially balanced by ocean circulation/overturning (green

243   arrows). The upper (lower) green arrow represents the volume flux out of the domain for

244   water with $\theta \leq 23°C$ ($\theta \leq 22°C$). Hence, the volume flux out of the purple region, equals the

245   difference between the green arrows. Both arrows are southwards because in this part of the

246   ocean the circulation consists of a strong northwards flow in a thin layer at the surface (higher

247   θ) and a weaker southwards flow in a thicker, deeper layer (lower θ). As we integrate up from

248   the lowest temperatures, the streamfunction itself is negative, but its vertical gradient is

249   negative at depth/low θ and positive at the surface/high θ .

250   Similar reasoning leads us to conclude that changes to the volume (mixing) in the

251   purple region are given by the difference in $\frac{\partial V}{\partial t}$ ($\frac{\partial D_{diff}}{\partial \theta}$) with respect to temperature.

252   To localise these quantities spatially, consider two nearby latitudes. Fig. 1(e) is

253   identical to 1(d) except an additional slab of ocean, to 18°N is added to the south, and the

254   yellow arrows represent the surface heat flux integrated from the North Pole down to the new

255   southern boundary ($F_{23°C, 18°N}$, $F_{22°C, 18°N}$). Evidently, the diapynal fluxes in the region between

256   18°N and 19.5°N (hollow arrows) are given by the difference between values of F at the two

257   different latitudes. Similar considerations apply to the overturning (green arrows) and to the

258   time derivative and mixing terms.

259

260   Note the resemblance of Eq (12) to the equation for the evolution of ocean

261   temperature (neglecting horizontal diffusion):

262

263    $$\frac{\partial T}{\partial t} = \frac{\partial}{\partial z}\left(K_v \frac{\partial T}{\partial z}\right) + \frac{I}{\rho_0 c_P} - \nabla.(\boldsymbol{u}T) .$$ (14)

264

265   Here K_v is the diffusion coefficient, $\boldsymbol{u}$ the three-dimensional ocean velocity and I is the

266   solar irradiance encountered earlier. The correspondence between the terms in Eqs (12) and

267   (14) becomes more obvious when we consider the surface boundary condition

268

269
$$K_v \frac{\partial \theta}{\partial z}\Big|_{z=0} = \frac{Q_{NET} - I_S}{\rho_0 C_P}.$$
       (15)

270

271   where Q_{NET}, the net surface heat flux and I_s, the surface irradiance were introduced

272   earlier. Recall that K_v consists of a background value, which increases with depth and a time-

273   varying part, which depends on stratification and velocity shear.

274

275   In the surface mixed layer K_v becomes large whilst $\partial \theta / \partial z$ is small and the surface

276   flux, $Q_{NET} - I_S$, is effectively spread over a vertical distance of the order of the mixed layer

277   depth. We shall use this property to develop a conceptual model in Section 3.6.

278

279   **3. Results**

280

281   **3.1 Ocean temperature response**

282

283   The global temperature response in the perturbed ensemble experiment is shown in

284   Fig. 2, a time-depth plot of horizontal averaged ensemble mean ocean temperature anomaly

285   relative to the mean of the 140-year control. In the first decade after the diffusivity is

286   increased, near-surface ocean temperatures (0-100m) decrease by ~0.15K, reaching a

287   minimum at year 8 (2 years before the diffusivity is returned to its original value – this is seen

288   in the unfiltered data (not shown) and is not an artefact of filtering). Simultaneously, the

289   subsurface ocean (below 100m) warms, with maximum warming at ~200m around year 9.

290   Thus, the change in mixing results in transfer of heat from the surface layer to the

291   thermocline, reminiscent of the observed hiatus of the 2000s. When the diffusivity is returned

292   to its original value at the beginning of year 11, the surface ocean warms, with peak surface

293   temperature occurring at year 15. In the subsurface ocean, there is slight cooling in the 200-

294   300 m depth interval, but below this the temperature remains roughly constant for the

295   remaining 10 years of the experiment. Hereinafter, we refer to years 1-10 of the ensemble

296   experiment as the hiatus period and years 11-20 as the surge period, although strictly this

297   should be defined in terms of anomalous global mean temperature tendency. The heat taken

298   up during the simulated hiatus period remains in the ocean for at least a decade after the

299   diffusivity has been restored to its original value. Although anomalously cool during the

300   hiatus, global mean SST becomes anomalously warm over the surge period.

301

302   Ensemble mean zonal average ocean temperature anomalies during years 6-10 (Fig.

303   3(a)) indicate cooling in the tropics-subtropics (30°S-30°N) from the surface to about 100m

304   and warming in the permanent thermocline throughout the tropics and midlatitudes, but

305   particularly marked in the tropics (20°S-20°N, 100-400m). This pattern of surface cooling and

306   deep warming is strongly reminiscent of the observed hiatus of the 2000s (e.g. Drijfhout et al.

307   2014).

308

309   During years 11-15 there is warming throughout the tropics and midlatitudes down to

310   1000m depth (Fig. 3(b)). However, weak cooling of the high latitudes present during years 1-

311   10 remains, particularly in the northern hemisphere to depths of 800m, but is counterbalanced

312   by a slight warming from 800-2500m (not shown). Once again, the heat taken up by the ocean

313   into the main thermocline during the hiatus period persists into the surge period.

314

315   Fig. 4(a) shows the ensemble mean SST anomaly averaged over years 6-10. Surface

316   cooling is particularly marked in the tropics. The western boundary current regions by

317   contrast, exhibit warming, albeit over a smaller area. A negative IPO-like pattern is apparent

318   with a wedge shaped region of cooling in the tropical Pacific, and warming in the western

319   north Pacific and the southeastern Pacific.

320

321   Following restoration of the diffusivity to its original value, the surface warms, with

322   Pacific SST showing a strongly positive IPO pattern averaged over years 11-15 (Fig. 4(b)).

323   Marked warming remains over the western boundary currents and their extensions in the

324   northern hemisphere, and the Indian ocean shows substantial surface warming. The Southern

325   Ocean, south western Pacific and south Atlantic show a weak cooling. Areas of statistically

326   significant warming during the surge are less extensive than areas of cooling during the

327   hiatus. However a clear global-scale pattern is evident.

328

329   The SST anomaly patterns can be compared to the 0-1000m ocean heat content

330   anomaly. During years 6-10 there are substantial rises in ocean heat content in the tropics and

331   subtropics (40°S - 40°N) which remain largely in place in years 11-15, that is, the uptake of

332   heat during the hiatus is not reversed during the surge (Fig. 4(c), (d)). Unlike the hiatus, the

333   surge SST anomaly pattern in years 11-15 echoes that of the ocean heat content anomaly over

334   much of the ocean: in the tropical and south Pacific, the Indian and the North Atlantic Oceans,

335   but not in the South Atlantic, the North Pacific, or the south west Pacific.

336

337   Turning to the ocean surface heat uptake anomaly (annual mean anomaly of net

338   surface heat flux into the ocean, Fig. 4(e), (f)), there are large increases in years 6-10

339   throughout the tropics and subtropics of all ocean basins, and in some subpolar regions. A

340   zonally banded structure is seen, seemingly related to oceanic fronts and mode water

341   formation regions with strong anomalies over the ITCZ and the western boundary currents

342   (particularly the Gulf Stream) and adjacent to Antarctica. When the diffusivity is returned to

343   its standard value in years 11-15, the ocean heat uptake anomaly reduces substantially across

344   the globe, but remains positive in many regions including the tropical Pacific and over the

345   Gulf Stream. The North Atlantic subpolar gyre by contrast shows a strong reduction in ocean

346   heat uptake during the surge period.

347

348   **3.2 Energy budget**

349

350   Fig. 5 indicates the impact of the perturbation on Earth's energy flows (Wild et al.

351   2013). There is no effect on incident solar radiation at the TOA hence this is not plotted. Fig.

352   5(a) shows the impact on the remaining shortwave (SW) flows. The reflected SW radiation at

353   the TOA (black) is initially reduced by 0.25 W m^{-2} (a 5-year filter is applied to the data), and

354   then gradually returns to its control value over the next 20 years. The atmospheric absorption

355   (red) is also initially reduced, but returns to the control value earlier, after about 12 years, and

356   overshoots slightly in the surge period. The reduction in both reflection and absorption by the

357   atmosphere means that the incident surface SW radiation (green, cyan) is increased by about

358   0.6 W m^{-2}, the change in surface reflection (blue) being negligible. The incident surface SW

359   radiation returns to its unperturbed value after about 12 years (2 years after the diffusivity

360   returned to normal).

361

362   The impact on non-solar energy flows is depicted in Fig. 5(b). Outgoing LW radiation

363   at the TOA (black) displays a symmetrical pattern with a reduction in the first 10 years

364   (consistent with reduced SST) and an increase in years 11-20 consistent with temperatures

365   warmer than the control. The biggest changes occur in the surface upwelling (red) and

366   downwelling (green) LW, which decrease by about 1 W m^{-2} relative to the control during the

367   hiatus, but increase rapidly by 2 W m^{-2} once the diffusivity returns to its control value. Thus

368   unlike the shortwave, the LW terms strongly overshoot their original values in the surge

369   regime. Of the turbulent heat flux terms, sensible heat (blue) shows negligible variation,

370   whilst latent heat (cyan) bears a strong resemblance to atmospheric absorption (weaker latent

371   heat loss and reduced SW absorption during the hiatus period may be linked via reduced

372   atmospheric humidity). Both the latter terms remain slightly higher than their control values

373   in the last 10 years of the perturbed simulations.

374

375   Global mean ocean heat uptake, net TOA heat flux and global mean heat content

376   tendency show very similar variation as required by energy conservation, since most of the

377   heat capacity resides in the ocean, hence only the ocean heat uptake is illustrated (Fig. 6). The

378   control displays large decadal fluctuations superimposed on a global net heat loss (TOA

379   imbalance) of about −0.2 W m^{-2} (vertical black line), indicative of long-term drift. This is

380   associated with the model Antarctic Bottom Water (see Fig. 10(a)) in the deep Southern

381   Ocean and is unlikely to affect the signals in the top 1000m seen in Figs. 2–4.

382

383   The diffusivity perturbation causes substantially increased ocean heat uptake of about

384   +0.6 W m^{-2} relative to the control. This elevated heat uptake declines steeply between years 8

385   and 12, and becomes indistinguishable from the control. The ocean heat uptake thus displays

386   an asymmetry: heat gained during the hiatus is not fully discharged from the ocean in the

387   subsequent surge (within the timescale of our experiments).

388

389   **3.3 Ocean and atmosphere surface temperature response**

390

391   The ensemble mean global average SST is plotted in Fig. 7 (red) together with the

392   global average SST from the control (vertical black line) and one ensemble member (green)

393   which was integrated for an extended period after the diffusivity was restored to its original

394   value. The mean SST over the 140-year portion of the control was 17.95 K. In response to the

395   reduced diffusivity, the ensemble mean global average SST reduces by about 0.15 K to

396   17.80°C. When the diffusivity is returned to its original value at the beginning of year 11,

397   global average SST increases steeply by ~0.25 K in 2-3 years, although strictly speaking, the

398   hiatus ended and the surge began when global temperature stopped declining and began to

399   rise around year 8 (this is seen in the unfiltered data (green) and is not an artefact of time

400   filtering). Subsequently the ensemble mean SST stabilizes at about 18.05 °C. The green curve

401   indicates the evolution of a single ensemble member rather than the ensemble mean, which

402   was integrated for a much longer period than the others. The surge in temperatures in years 8-

403   12 leaves the global mean SST higher than the control, possibly for several decades or more.

404   During the surge and hiatus periods the ensemble mean SST is significantly (95% confidence)

405   below/above the control, but the ensemble spread remains similar to the temporal variability

406   of the control. In contrast in the transition period (years 10-12), the SST anomaly is not

407   significantly different from the control, but the ensemble spread is smaller than the control

408   variability. This suggests a potentially high predictability of this transition phase.

409

410   Fig. 8 provides a scatter plot of annual mean SAT versus SST for the control (red

411   circles) and the individual ensemble members for the first ten years of each simulation (black)

412   and the last ten years (blue). SAT correlates very well with SST so a hiatus in SST is

413   equivalent to one in SAT on an annual mean and global average basis. The same linear

414   relationship between SST and SAT seen in the control holds for both surge and hiatus

415   periods. Spatial and seasonal differences in this relationship are of interest, but are not

416   pursued further in this paper.

417

418   **3.4 Analysis in temperature space**

419

420   A consistent finding is that following the relaxation of conditions that force a hiatus,

421   the surface warms rapidly and remains warmer than the previous long-term average state. We

422   now investigate this behavior using water mass transformation analysis.

423

424   *(i) Watermass transformation*

425

426   We first apply the water mass transformation framework, Eqs. (12), (13), to the

427   control simulation. The net trend $\partial V/\partial t$, Fig. 9(a), is very small in most temperature classes

428   and latitudes, but $\partial^2 V/\partial t\partial\theta$ is negative between 0-2°C (80°S-20°N) representing a loss of

429   volume. This is counterbalanced by positive $\partial^2 V/\partial t\partial\theta$ at the same latitude range, between -

430   2-0°C representing a gain in volume. Thus there is cooling in the deep Southern Ocean

431   (~0°C) consistent with the overall negative TOA balance.

432

433   From Eq (12) surface fluxes, ocean circulation and mixing compete to create a net

434   trend in the volume of seawater in temperature classes. In Fig. 9(b)-(d) each panel shows one

435   term from Eq (12). Values plotted for each latitude, ϕ, and temperature, θ, represent all the

436   fluid with temperature$\leq\theta$ and north of ϕ. Therefore, as with streamfunction plots in depth-

437   latitude space, a convergence/divergence of isolines represents accumulation/loss of volume

438   at a particular θ, ϕ. Along isolines, input and output cancel – water transformed from the class

439   (and/or latitude) below is counterbalanced by the same amount of water being transferred to

440   the class (and/or latitude) above. Hence we can draw arrows connecting sources of water with

441   particular properties to sinks, or closed loops representing continuous transformation

442   pathways. The reader should remember that the 2D temperature-latitude plots in Fig. 9

443   represent complex water pathways in 3D physical space (Fig. 1)

444

445   Fig. 9(b) shows the overturning streamfunction, ψ, in temperature space (Eq. (1)). It is

446   calculated by integrating up lateral transports of fluid of various temperatures, so in principle

447   the diagnosed apparent "vertical" diathermal motion may be associated with volume trends

448   $\partial V/\partial t$ rather than actual warming or cooling. However, since the trends are weak, (Fig. 9(a))

449   the diagnosed diathermal motion should be accurate. Negative (positive) values indicate

450   clockwise (anticlockwise) transformation cells. Shallow subtropical cells (STCs), 25-30Sv in

451   strength, are apparent, centered at about 22°C, 10°S in the southern hemisphere and, slightly

452   cooler, 20°C, 10°N in the north. These deliver cold water upwelled near the equator (sharp

453   gradient between 15-25°C at 0° latitude implies transfer from cold to warm temperatures as

454   explained in Section 2.2) to the downwelling/subduction regions in the subtropics (Fig. 1

455   gives a 3D view of this process). The model North Atlantic Deep Water (NADW) cell (i.e. the

456   AMOC) carries ~25Sv of surface waters northwards into the North Atlantic and returns cold

457   (3-7°C), deep waters southwards. These upwell at mid-high southern latitudes (~40°S) and

458   rejoin the surface circulation. The Antarctic Bottom Water (AABW) cell downwells ~25Sv of

459   cold surface waters in the Southern Ocean and carries them northward as near-bottom

460   currents (at ~0°C). These rise and warm slightly at mid-high latitudes in the northern

461   hemisphere and join the NADW, making their way back southwards.

462

463   Air-sea fluxes directly transform water shifting it from one temperature class to

464   another. The associated streamfunction, F, (Eq. (10)) is analogous to ψ (Fig. 9(c)); but differs

465   in that it is defined from the (known) diathermal flux; it gives diagnosed (unrealistic)

466   horizontal transports consistent with weak volume trends and no mixing. Air-sea fluxes only

467   act on a temperature class if the bounding surface of that class reaches to the surface at the

468   latitude in question (or close enough that penetrative solar radiation passes through its

469   boundary) as illustrated (section 2.2) by the purple region of Fig 1(d). Thus there is a blank

470   region in Fig. 9(c) between 40°S and 30°N below 10°C where air-sea fluxes cause no

471   temperature change. Air-sea fluxes can make warm waters even warmer (tropical heating) and

472   cool waters even cooler (subtropical/high latitude cooling). Water in the 23°C range is

473   transformed by air-sea fluxes into warmer waters (up to 30°C) mainly in the tropics. Waters

474   in this class are also cooled by air-sea fluxes between the subtropics and mid latitudes to

475   temperatures around 15°C. Further poleward, waters around 5°C are transformed into cold

476   deep water below 0°C, largely in the Southern Ocean and the North Atlantic.

477

478   Mixing, obtained as a residual, $(\partial D_{diff}/\partial\theta)$, in Eq. (12) opposes air-sea fluxes,

479   removing extremes of temperature and adding volume to intermediate temperature classes

480   (Fig. 9(d)). However, mixing also acts within the ocean interior, where air-sea fluxes cannot

481   penetrate, for example mixing is active between the Equator and 40°S transforming water

482   from the 15°C to the 20°C range, and balances the NADW overturning cell at around 50°N

483   where waters between 5-10°C are transformed into the range 0-5°C.

484

485   *(ii) Transformation and formation rates*

486

487   We now focus on the tropics and subtropics where a large part of the surge signal

488   originates, and examine the horizontal derivative of the transformation rate. Following Eq.

489   (12), in Fig. 10(a) we display the latitudinal divergence of the volume flux across isotherms

490   (the transformation rate) at the Equator (averaged over 3°S–3°N) as a function of temperature

491   due to air–sea fluxes, mixing, overturning and volume change. This is essentially a section

492   through Figs 9(a)–(d) at the Equator, differentiated with respect to latitude. We plot curves for

493   the control simulation to elucidate the fundamental balances in the model and subsequently

494   investigate how these balances change during the hiatus and surge in the perturbed ensemble.

495

496   At the Equator, air–sea fluxes (green) cause transformation in temperature classes 17–

497   32°C (there is no direct effect on isotherms below 17°C as these do not outcrop at the

498   Equator). The lines have a negative gradient (formation rate) between 26-31°C, hence air–sea

499   fluxes tend to generate water masses in this temperature range (F has a negative sign in eq.

500   (12)). Between 17-25°C, the lines have a positive gradient and air–sea fluxes remove water in

501   these classes. The overturning (red) acts to remove (add) water between 23-30°C (10-23°C).

502   Mixing (blue) differs from the other terms as the associated formation rate has three regimes:

503   between 28-32°C mixing removes water; between 21-28°C it adds water; and between 10-

504   21°C it removes water. This is consistent with mixing tending to eliminate extremes. The

505   result is that at the Equator there are four thermal regimes. In each, two out of the three terms

506   (in formation rate) are in approximate balance and the third is relatively unimportant. Thus

507   between 28–32°C the predominant balance is mixing versus air–sea fluxes (Equatorial regime

508   iv); between 25-28°C mixing versus overturning (regime iii); between 21-25°C mixing versus

509   air–sea fluxes (regime ii); and between 10-21°C mixing versus overturning (regime i). Below

510   15°C there is little coherent signal. In all four regimes, mixing is one of the dominant terms.

511   Volume change is a very small term over most temperature classes, averaged over the 140-

512   year control simulation.

513

514   Fig. 11(b) shows transformation rates for the off-Equatorial regions (average over 18–

515   12°S and 12–18°N – the strongest subsurface anomalies in Fig. 4 are between 20°S-20°N).

516   Transformation rates are much smaller compared to the Equator: 1–2Sv/°latitude compared to

517   8–10Sv/°latitude and the roles of the individual processes differ. Air–sea fluxes add volume

518   between 28-32°C, and between 20-25°C, and remove volume between 25-28°C. The

519   overturning behaves in an opposite manner than at the Equator, adding volume between 25-

520   28°C and removing it between 20–25°C. Mixing removes volume between 28-32°C (off-

521   Equatorial regime iv) and adds it between 20-25°C (regime iii).   Between 10°C-20°C,

522   overturning and mixing balance, mixing adding volume and overturning removing it (regime

523   ii). The situation is reversed between 5°C-10°C with overturning adding volume and mixing

524   removing it (regime i). Details vary between the northern and southern off-Equatorial regions

525   (not shown), but the regimes are similar. Again, net volume change is a very small term.

526   Although the thermal regimes are different from those at the Equator, the boundaries between

527   the regimes occur at about the same temperatures.

528

529   In both Equatorial and off-Equatorial regions, the corresponding formation rate curves

530   for the perturbed ensemble (not shown) are similar in shape to the control and the boundaries

531   between the thermal regimes occur at the same temperatures.

532

533   We further characterize the thermal regimes by calculating the formation rate terms

534   (Section 2.2 and Fig. 1) for the control simulation. Fig. 11(a)shows the net volume flux

535   convergence for each regime i–iv, associated with overturning (red), air–sea fluxes (green)

536   and mixing (blue) in the Equatorial region. The net volume inflation in each of these regimes

537   is very small, and there is a near-exact balance between the three terms. In regime iv, air–sea

538   fluxes create about 6Sv/°latitude of water (36Sv in total for the 3°S–3°N region) whilst

539   mixing and overturning remove 4Sv/°latitude and 2Sv/°latitude respectively. Mixing delivers

540   3Sv/°latitude of water into regime iii, largely balanced by overturning. Regime ii is

541   effectively a reversed version of regime iv (loss of ~ 6Sv/°latitude by air–sea fluxes, gain of

542   4Sv/°latitude and 2Sv/°latitude by mixing and overturning respectively). Similarly regime i is

543   a reversed version of regime iii. This suggests that regimes i and iii and ii and iv are causally

544   connected. The situation is subtly different in the off-Equatorial regions (Fig 11b) where

545   regimes iii and iv both have mixing balancing overturning and air–sea fluxes, but with

546   opposite signs. Similarly, regimes i and ii both have mixing largely balancing overturning, but

547   with opposite signs.

548

549   In both Equatorial and off-Equatorial regions, there are regimes where air–sea fluxes

550   add volume and others where they remove it, suggesting that the regimes are not all stacked

551   vertically, but more likely horizontally (e.g. warming in the western subtropics and cooling in

552   the eastern). This would explain the causal connection between off-Equatorial regimes iii and

553   iv for example if the spatial regions corresponding to these regimes are connected by

554   atmospheric or oceanic teleconnections. Fig. 1(d), depicting a strong east-west temperature

555   gradient in the near-surface of the northern tropical Pacific, supports this conjecture. Albeit

556   only for a single month from one ensemble member, it suggests that above the 20°C isotherm,

557   off-Equatorial regimes ii-iv are stacked east-west and linked by the northern STC.

558

559   *(iii) Changes of volume in temperature classes*

560

561   Fig. 12 shows the logarithm of the ratio (ensemble mean ÷ control mean) of the

562   globally integrated volume in temperature space, calculated in 1K intervals and based on

563   monthly means, with a 12–month boxcar filter applied to smooth the data (before taking the

logarithm). Negative (positive) values indicate reduced (increased) volume in temperature

classes in the ensemble mean versus the control. In years 1-10 of the perturbed simulations,

there is a depletion of water in the range 27–30°C. Conversely there is a small increase in

volume at cooler temperatures, confined mainly to 25–27°C for the first five years, but

subsequently extending to cooler temperatures (down to 15°C). From year 11 onwards there

is an abrupt increase in the volume of the warmest waters, 27–30°C and a reduction of

volume in the 25–27°C range. The volume of water in the 18–25°C range decreases more

gradually, and in the 15–16°C range there is no reduction at all; indeed there is a long term

increase in the volume of these waters with little sign of impending decrease a decade after

the surge began. There are also notable increases of volume at around 10°C, still present at

year 20. The increase in volume in the –1–0°C range is a reflection of the drift in the control

associated with the long term negative TOA imbalance of –0.2 W m^{-2}.

Extending the plots to cover latitude, the logarithm of the absolute volume per unit

latitude for temperature classes in the control simulation (Fig. 13(a)) shows the largest

volume of seawater in the coldest temperature classes, and a comparatively low volume in the

warmest classes (black lines indicate the zonal and time average SST ±1 standard deviation at

each latitude).

Fig. 13(b) shows the logarithm of the ratio (ensemble mean ÷ control mean) of

globally integrated volume for the first (blue) and second (red) decades of the perturbed

simulations. Negative (positive) values indicate a loss (gain) of volume compared to the

control. In the first decade there is a strong decrease in volume above 25°C and a

compensating, but more modest increase in the 15-25°C layer. In years 11–20 the warmer

layers regain some of the volume that was lost in the hiatus decade at the expense of loss in

589   volume of waters between 20-25°C; however the volume gained between 15- 20°C is retained

590   in the subsequent surge and new equilibrium period. The 15°C and 10°C volume classes in

591   particular remain much thicker than in the control in years 11–20.

592

593   Next we examine the change in volume per unit latitude in temperature classes as a

594   function of latitude for the hiatus (years 1–10) and the surge (years 11–20). In years 1–10

595   (Fig. 13(c)) there is considerable loss of volume of the warmest tropical waters (> 25°C)

596   between 20°S and 20°N. Below these waters we note an increased volume of waters between

597   15-25°C, extending poleward to 30°S/30°N, slightly greater in latitudinal extent than the

598   surface cooling/loss of volume. There is also increased volume of the warmest waters in the

599   Southern Ocean (80–40°S) and the northern midlatitudes (20–50°N).

600

601   In year 11–20 (Fig. 13(d)), we see a widespread increase in volume of the warmest

602   waters, including a large increase in the tropics where the volume was previously depleted.

603   The Southern Ocean remains as warm during the surge period as it was during the hiatus, but

604   the northern midlatitudes see a very strong increase in the volume of warmer waters. At

605   temperatures between 20–25°C, the extra volume deposited during the hiatus is lost, but

606   below 20°C the increased volume of water gained at the expense of the warmest waters

607   remains throughout the subsequent surge and the new equilibrium period.

608

609   In Figs 13(c) and (d) we have superimposed the circulation cells from Fig 9(b). These

610   demonstrate that the warming of the waters warmer than about 15°C during the hiatus in years

611   1-10 coincides with the positions of the subtropical cells. The warming and cooling pattern

612   north of 40°N seems associated with the AMOC.

613

614   Finally we investigate pentadal changes to the formation rate in the thermal regimes in

615   the perturbed ensemble (Fig. 14) in order to explain the changes in volume seen in Figs. 12

616   and 13. At the Equator, across all regimes, during the hiatus the changes to the mixing (blue)

617   create anomalies in the overturning and surface heat fluxes (Fig. 14(a), (b)). The overturning

618   anomalies die down in the early part of the surge (Fig. 14(c)) and completely disappear in the

619   second pentad (Fig. 14(d)), leaving a modified balance in the long term where the mixing

620   remains changed, but is balanced by a modified surface heat flux. There is a suggestion that

621   regimes ii and iv, and i and iii are opposite to each other in the final pentad.

622

623   A similar pattern occurs in the off-Equatorial regions where the changes in mixing

624   during the hiatus induce changes in the ocean circulation (Fig. 14(e), (f)), which however die

625   down and disappear during the surge (Fig. 14(g), (h)). The final state once again pitches long

626   term changes in mixing against changes in air–sea fluxes and regimes iii and iv mirror each

627   other, reinforcing the earlier suggestion that there is a causal connection between them (Fig.

628   11).

629   We defer detailed analysis of the mechanism governing this transient behaviour to a

630   future study, however we link the behaviour in temperature space in Fig. 14 to depth space

631   and previous studies (e.g. England et al. 2014) by plotting the pentadal evolution of the STCs

632   (Fig. 15(a)-(d)). The thin contours show the meridional overturning streamfunction from the

633   control simulation in the tropical (30°S-30°N) Indo-Pacific. There is a ~30Sv clockwise cell

634   in the northern tropics/subtropics and a somewhat stronger (~40 Sv) anticlockwise cell in the

635   Southern Hemisphere. Both have a meridional extent of ~25° of latitude, with the southern

636   cell extending slightly deeper (~300 m compared to ~200 m for the northern cell).

637   In the first pentad (hiatus, Fig. 15(a)) we see a modest strengthening of the southern

638   cell, but in the second there is a much bigger strengthening (order 5 Sv) of the northern cell

639   (Fig. 15(b)). In the third pentad (surge, Fig. 16(c)) the northern cell returns to normal strength,

640   whilst the southern cell weakens by ~5 Sv. In the fourth (Fig. 15(d)) and consistently with

641   Figure 14, we find both STCs have returned to normal. Note that when only one of the

642   overturning cells increases, we are likely to see opposing changes in the Equatorial versus the

643   off-Equatorial regions (e.g. in regimes iii and iv the red bars are of opposite sign between the

644   Equatorial and off-Equatorial regions), since increasing divergence at the Equator is

645   associated with increasing convergence off-Equator and *vice-versa*.

646   Consistent with previous studies (Meehl et al. 2013), increased heat drawdown in the

647   ocean is associated with strengthening STCs, and the reverse is true for surge conditions.

648   Thus, whilst the perturbed background diffusivity artificially induces a hiatus in our ensemble

649   experiment, heat uptake in the 300 m layer increases due to a realistic physical mechanism.

650   The   stronger/weaker   STCs   in   Figs.   15(b),   (c)   are   in   addition   associated   with

651   strengthened/weakened easterly trade winds (Figs. 15(f), (g)). In contrast there is no marked

652   signal in the wind stress when the STC's are near normal (Figs. 15(e), (h)). Therefore ocean

653   heat uptake and climate variability feed back on each other and artificial changes to the

654   background diffusivity induce a physically realistic circulation response in line with previous

655   studies.

656

657   **3.5 Conceptual model of transition**

658

659   The previous section demonstrated that, in the model, mixing is always of first order

660   importance in the thermal balance in the tropics and subtropics (Figs. 10 and 11). Combining

661   this result with the fact that the temperature tendency due to mixing is proportional to the 2nd

662   derivative of the temperature (Eq. (14)), we hypothesize that any modification to one of the

663   forcing terms will modify the temperature leading to changes in stratification, and bringing

664   the mixing term back into balance with its antagonist.

665

666   Consider an idealized upper ocean consisting of a 200m layer in which surface heating

667   (I) is balanced by diffusion $(\partial(K_v \partial\theta/\partial z)/\partial z)$ similar to regime iv, Fig. 10(a), with the

668   further simplification that ocean heat transport divergence, $\nabla.(\boldsymbol{u}T)$, is identically zero. We

669   apply a uniform heating of 20 W m^{-2} distributed evenly throughout the upper 80m

670   representing solar input. Initially, we specify zero heat flux through the surface boundary,

671   relying on the upper ocean heating to drive the model to equilibrium. We use the diffusive

672   heat flux at the lower boundary to drive a deeper layer of thickness 100m balanced by a fixed

673   ocean heat transport divergence of 20 W m^{-2}. This deeper layer is thus similar to regime iii in

674   Fig. 10(a.)

675

676   The upper 200m is discretized with a forward timestepping scheme and standard

677   second order accurate finite differences in the vertical (timestep Δt=864s, vertical grid

678   spacing Δz=1m). The lower 100m is treated numerically as a single layer. We assume a

679   constant background diffusion coefficient K_v=5x10^{-5} m^2 s^{-1}, set the initial temperature to 20°C

680   in all the layers, then integrate the model forward for 120 years. At the beginning of year 121

681   the background diffusivity is increased by 20% to 6x10^{-5} m^{2}s^{-1} and in addition, heat flux

682   feedback to the atmosphere is switched on (Eq. 15), damping the SST back to the long term

683   mean (based on years 40-80) with a feedback parameter of 1 W m^{-2} K^{-1}. At the beginning of

684   year 131, the background diffusivity is returned to its standard value, but the surface heat flux

685   feedback is retained and the model is integrated for a further 30 years.

686

687   The system evolves to equilibrium in about 20 years such that diffusion transports heat

688   downward from the surface (where it is input by heating) to the deepest layer where it is

689   removed by heat transport divergence and continues without significant change until year

690   120. When the diffusivity is increased at the beginning of year 121, there is an immediate

691   elevation of the isotherms above 140m and a depression of isotherms below, resulting in a

692   cold (warm) anomaly above (below) 140m depth (Fig. 16(a)), i.e. a hiatus.

693

694   When the diffusivity is returned to normal at the beginning of year 131, the system

695   experiences a temporary perturbation such that the export of heat by mixing from the upper

696   ocean through the lower boundary is reduced. There is thus a temporary imbalance in favour

697   of the surface heat flux, which modifies the temperature gradient to restore a balanced regime

698   (note that although we perturbed the system by changing the diffusion coefficient, we could

699   have modified one of the other processes, advection or air–sea fluxes to create the hiatus).

700

701   This behavior is very reminiscent of Fig. 2, albeit with larger anomalies as it is

702   intended to represent behavior near the Equator rather than an average over the globe. In Fig.

703   16(b) temperature anomaly profiles with depth are plotted before and after the hiatus–surge

704   transition. The hiatus state (red) shows a ~0.7K reduction in temperature at the surface and a

705   corresponding increase at 200m. The cyan line shows how the temperature profile changes at

706   year 145 when the diffusivity has been reduced to its original value. A surface temperature

707   increase of a 0.2K over control values, with little depth variation is seen. This final

708   equilibrium state thus has a similar temperature gradient to the pre-hiatus state in the top 200

709   m, but is systematically warmer at all depths.

710

711   We now compare the zonally averaged response in the full climate model with this

712   conceptual model. Fig. 16(c) shows the ensemble mean zonal average (confined to the Pacific

713   basin) of the temperature in the top 200m of the Equatorial Pacific (3°S–3°N) in the full

714   climate model. We have noted previously that the major temperature anomaly during the

715   simulated hiatus sits below 200m and remains there during the surge. During the hiatus (red

716   line, representing an average of years 6–10 of the ensemble experiment), temperature above

717   120m reduces by up to 0.5K, whilst below this there is a temperature increase of a similar

718   magnitude. In the first year of the surge (cyan line, average over year 11), temperature at

719   200m stays at the same elevated level attained during the hiatus. Above this depth there is an

720   increase in temperature of 0.4K, approximately independent of depth. Hence in the surge

721   simulated by the climate model, as in the conceptual model, the temperature gradient returns

722   to pre-hiatus values, but the temperatures themselves are elevated due the increased

723   temperature of the deep layer.

724

725   The northern off-Equatorial region, 12–18°N, (16(d)), displays similar behavior to that

726   at the Equator. Here,the cyan lines are plotted for year 3 of the surge (not year 1) because it

727   takes longer for the system to attain equilibrium away from the Equator (varying Rossby

728   wave speed is the likely explanation). The southern off-Equatorial region displays the same

729   behavior, except the warming during the hiatus occurs deeper down at 400m (not shown).

730

731   Interestingly, in the conceptual model (Fig. 16(b)) we only had to increase the

732   diffusion coefficient by 20% to achieve a realistic response, whereas in HadCM3 we applied a

733   100% increase. Beyond the simplification inherent to the conceptual model, it is possible that

734   this mismatch comes from other sources of mixing in HadCM3, such as numerical mixing and

735   shear driven instability (e.g. Megann (2018)).

736

4 Conclusions and Discussion

738

739   We performed sensitivity experiments using the HadCM3 climate model to
740 understand decadal changes in the rate of global warming. Specifically, we increased the
741 ocean heat uptake by increasing the vertical diffusivity in the model for 10 years, before
742 returning vertical diffusivity to normal values. The main conclusions are as follows:

743

744   •   Experiments with increased ocean diffusivity show Pacific-dominated
745   hiatus-like behavior: the Pacific undergoes a transition to a negative Inter-decadal
746   Pacific Oscillation like state. Outgoing longwave radiation at the Top of the
747   Atmosphere, oceanic latent heat loss and surface upwelling and downwelling
748   longwave radiation are all strongly reduced due to reduced surface temperatures,
749   however the ocean absorbs more shortwave radiation due to reduced atmospheric
750   absorption.

751   •   When ocean vertical mixing is increased global surface temperature
752   decreases, i.e. the climate is forced into a hiatus-like state. When ocean vertical
753   mixing returns to normal values the surface temperature increases, and overshoots the
754   climatological values, i.e. a surge occurs.

755   •   The climatological thermal balance in the warmest (near surface)
756   waters of tropical Pacific Ocean is maintained by mixing balancing surface heat flux.
757   In contrast in the cooler layer below mixing is balanced by ocean heat transport
758   divergence. Related, but slightly different balances prevail in the off-Equatorial
759   regions.

760   •   The overshoot into surge conditions is due to long term depression of

761   deep (~15°C) isotherms following the hiatus (put simply, the ocean has no mechanism

762   to quickly remove the heat deposited at depth). In order to maintain thermal balance,

763   the upper layer temperature, the most responsive variable, must rise to higher than

764   normal values, via increased surface heat input in order to restore the thermal gradient,

765   which supports mixing (see schematic, Fig. 17).

766   •   Other things being equal, the changes in stratification caused by a

767   hiatus increases the probability that a subsequent surge will occur

768

769   Due to our use of fundamental thermal balances in this study, we are confident that

770 our conclusions are correct in their essentials. However there are some caveats to consider:

771

772   •   We have used one particular model of relatively coarse resolution

773   (although it maintains a very stable climate similar to the present day).

774   •   The thermal balances may differ quantitatively from model to model.

775   •   Our model does not resolve ocean mesoscale eddies which play an

776   important role in the thermal balance of the ocean (Griffies et al. 2015). In mitigation

777   our model employs the Gent McWilliams eddy parameterization scheme.

778   Our results are consistent with previous observational and modelling studies, in

779 particular, Maher et al. (2018). The authors modified Pacific trade winds to induce a hiatus in

780 a similar way to our modification of the mixing, and show similar results in terms of the

781 changes in subtropical cells, heat content, the transfer of excess heat to the Indian Ocean and

782 the legacy of anomalously high heat content even under a reversal of the perturbation. This

783 agreement as well as our Figs 14 and 15, suggest a tight coupling between the three

784 competing processes of surface fluxes, wind-driven ocean circulation and mixing, identified

785   in the present study. Similarly, observations (Nieves et al. 2015) confirm the transfer of heat

786   during the recent hiatus period to the Indian Ocean.

787

788   Finally we consider the wider implications of our findings. As is widely appreciated,

789   when the deep ocean is heated on decadal timescales, the additional heat cannot easily and

790   quickly be returned to the atmosphere. We have shown that this additional heat has a legacy

791   impact on the global mean surface temperature on decadal and longer timescales. The

792   additional heat uptake during hiatus periods (which is well attested) conditions the earth

793   system to warm even more strongly when the hiatus ends. Whilst we have engineered a hiatus

794   by modifying the vertical mixing, in principle we would expect to see the same behavior if the

795   heat enters the deep ocean by other means (e.g. via modification of the shallow overturning

796   cells from windstress perturbations, or changes to the surface heating and subsequent

797   subduction, mechanisms which have been hypothesized to have driven the early 2000s

798   hiatus).   Idealized/conceptual one-dimensional models of Earth's energy balance do not

799   currently include the effects described in this paper.

800

801   Our results also have important implications for decadal and longer predictions using

802   model based forecast systems. In particular we suggest that accurate initialization of the

803   subsurface ocean may be a key element of such systems as inaccuracies could result in

804   erroneous predictions of hiatus or surge conditions (consistently with the findings of Sévellec

805   and Federov, 2017, and Germe et al., 2018). Similarly, inaccurate simulation of forced hiatus

806   periods could lead to systematic biases or additional uncertainty in centennial climate

807   projections.

808

809   Further work should establish the robustness of our result in a wider variety of models

810   (including at higher ocean resolution). The watermass transformation method we used could

811   also in principle be applied to observational data, although in practice great care would be

812   needed to take into account of observational uncertainties and internal variability.

813

814   **Acknowledgements**

815

822

823   **References**

824
825   Chen, X., and K.-K. Tung, 2014: Varying planetary heat sink led to global-warming

826   slowdown and acceleration. *Science,* **345**, 897-903, doi: 10.1126/science.1254937.

827   Drijfhout, S. S., A. T. Blaker, S. A. Josey, A. J. G. Nurser, B. Sinha, and M. A.

828   Balmaseda, 2014: Surface warming hiatus caused by increased heat uptake across multiple

829   ocean basins. *Geophys. Res. Lett*., **41**, 7868-7874, doi.org/10.1002/2014GL061456.

830   England, M. H., and Coauthors, 2014: Recent intensification of wind-driven

831   circulation in the Pacific and the ongoing warming hiatus. *Nat. Clim. Change*, **4**, 222– 227,

832   doi:10.1038/nclimate2106.

833   Farneti, R., A. Dwivedi, F. Kucharski, F. Molteni, and S. M. Griffies, 2014: On

834   Pacific Subtropical Cell Variability over the Second Half of the Twentieth Century. *J. Clim*.,

835 **27**, 7102-7112, doi: 10.1175/JCLI-D-13-00707.1

836 Gastineau, G., A. Friedman, M. Khodri, and J. Vialard, 2019: Global ocean heat

837 content redistribution during the 1998-2012 Interdecadal Pacific Oscillation negative phase.

838 *Climate Dynamics*, **53**, 1187-1208.

839 Germe, A., F. Sévellec, J. Mignot, A. V. Fedorov, S. Nguyen, and D. Swingedouw,

840 2018: The impacts of oceanic deep temperature perturbations in the North Atlantic on decadal

841 climate variability and predictability. *Climate Dynamics*, **51**, 2341-2357.

842 Gordon, C., C. Cooper, C. A. Senior, H. Banks, J. M. Gregory, T. C. Johns, J. F. B.

843 Mitchell, and R. A. Wood, 2000: The simulation of SST, sea ice extents and ocean heat

844 transports in a version of the Hadley Centre coupled model without flux adjustments. *Climate*

845 *Dynamics*, **16**, 147-168, doi.org/10.1007/s003820050010.

846 Guemas, V., F. J. Doblas-Reyes, I. Andreu-Burillo, and M. Asif, 2013: Retrospective

847 prediction of the global warming slowdown in the past decade. *Nat. Clim. Change,* **3**, 649–

848 653.

849 Griffies, S. M., and Coauthors, 2015: Impacts on Ocean Heat from Transient

850 Mesoscale Eddies in a Hierarchy of Climate Models. *J. Climate*, **28**, 952-997,

851 https://doi.org/10.1175/JCLI-D-14-00353.1.

852 Hedemann, C., T. Mauritsen, J. Jungclaus, and J. Marotzke, 2017: The subtle origins

853 of surface-warming hiatuses. *Nat. Clim. Change*, **7**, 336-339.

854 Kosaka, Y., and S.-P. Xie, 2013: Recent global-warming hiatus tied to equatorial

855 Pacific surface cooling. *Nature*, **501**, 403-407.

856 Lee, M.-M., A. C. Coward, and A. J. G. Nurser, 2002: Spurious diapycnal mixing of

857 the deep waters in an eddy-permitting global ocean model. *J. Phys. Oceanogr.*, **32**, 1522–

858 1535.

859   Lee, S.-K., W. Park, M. O. Baringer, A. L. Gordon, B. Huber, and Y. Liu, 2015:

860 Pacific origin of the abrupt increase in Indian Ocean heat content during the warming hiatus.

861 *Nat. Geo*., **8**, 445-450.

862   Liu, W., S.-P. Xie, and J. Lu, 2016: Tracking ocean heat uptake during the surface

863 warming hiatus. *Nature Communications*, **7**, 10926.

864   Maher, N., M.H. England, A. Sen Gupta, and P. Spence, 2018: Role of Pacific trade

865 winds in driving ocean temperature during the recent slowdown and projections under a wind

866 trend reversal. *Climate Dynamics*, **51**, 321-336, https://doi.org/10.1007/s00382-017-3923-3.

867   Megann, A. 2018: Estimating the numerical diapycnal mixing in an eddy-permitting

868 ocean model. *Ocean Modelling*, **121**, 19–33, doi:10.1016/j.ocemod.2017.11.001.

869   Meehl, G., J. Arblaster, J. Fasullo, H. Aixue, and K. Trenberth, 2011: Model-based

870 evidence of deep-ocean heat uptake during surface-temperature hiatus periods. *Nature Clim

871 Change,* **1,** 360–364, doi:10.1038/nclimate1229.

872   Meehl, G.A., A. Hu, J. M. Arblaster, J. Fasullo, and K E. Trenberth, 2013: Externally

873 forced and internally generated decadal climate variability associated with the Interdecadal

874 Pacific Oscillation, *J. Climate*, **26**, 7298-7310, doi: http://dx.doi.org/10.1175/JCLI-D-12-

875 00548.1.

876   Meehl, G. A., H. Teng, and J. M. Arblaster, 2014: Climate model simulations of the

877 observed early-2000s hiatus of global warming. *Nat. Clim. Change,* **4**, 898–902.

878   Moat, B. I., B. Sinha, S. A. Josey, J. Robson, P. Ortega, F. Sévellec, N. P. Holliday,

879 G. D. McCarthy, A. L. New, J. J.-M. Hirschi, 2019: Insights into decadal North Atlantic sea

880 surface temperature and ocean heat content variability from an eddy-permitting coupled

881 climate model. *J. Climate*, **32**, 6137-6161, doi.org/10.1175/JCLI-D-18-0709.1

882   Nieves, V., J. K. Willis, and W. C. Patzert, 2015: Recent hiatus caused by decadal

883 shift in Indo-Pacific heating. *Science* **349**, 532-535, doi:10.1126/science. Aaa4521 (2015).

884   Nurser, A. J. G., R. Marsh, and R. G. Williams, 1999: Diagnosing water mass

885   formation from air– sea fluxes and surface mixing. *J. Phys. Oceanogr.,* **29**, 1468–1487,

886   doi:10.1175/1520- 0485(1999)029¡1468:DWMFFA¿2.0.CO;2.

887   Risbey, J., 2015: Free and forced climate variations. *Nature,* **517,** 562–563,

888   doi:10.1038/517562a.

889   Sévellec, F., B. Sinha, and N. Skliris, 2016: The rogue nature of hiatuses in a global

890   warming climate, *Geophys. Res. Lett.*, 43, 8169-8177.

891   Sévellec, F. and A. V. Fedorov, 2017: Predictability and decadal variability of the

892   North Atlantic ocean state evaluated from a realistic ocean model. *J. Climate*, **30**, 477-498.

893   Sévellec, F. and S. S. Drijfhout, 2018: A Novel Probabilistic Forecast System

894   Predicting Anomalously Warm 2018-2022 Reinforcing the Long-Term Global Warming

895   Trend. *Nature Communications*, **9**, 3024, doi:10.1038/s41467-018-05442-8

896   Smith, D., and Coauthors, 2015: Earth's energy imbalance since 1960 in observations

897   and CMIP5 models. *Geophys. Res. Lett*., **42**, 1205-1213, doi.org/10.1002/2014GL062669.

898   Song, Y., Y. Q. Yu, and P. F. Lin, 2014: The hiatus and accelerated warming decades

899   in CMIP5 simulations. *Adv. Atmos. Sci.*, **31**, 1316–1330, doi: 10.1007/s00376-014-3265-6.

900   Tanaka, Y., I. Yasuda, and H. Hasumi, 2012: Effects of the 18.6-yr Modulation of

901   Tidal Mixing on the North Pacific Bidecadal Climate Variability in a Coupled Climate

902   Model. *J. Climate*, **25**, 7625-7642, doi.org/10.1175/JCLI-D-12-00051.1.

903   Walin, G., 1982: On the relation between sea-surface heat-flow and thermal

904   circulation in the ocean. *Tellus A*, **34**, 187–195, doi:10.1111/j.2153-3490.1982.tb01806.x.

905   Watanabe, M., H. Shiogama, H. Tatebe, M. Hayashi, M. Ishii, and M. Kimoto, 2014:

906   Contribution of natural decadal variability to global warming acceleration and hiatus. *Nature*

907   *Climate Change*, 4, 893-897.

908   Wild, M., D. Folini, C. Schär, N. Loeb, E. G. Dutton, and G. König-Langlo, 2013: The

909 global energy balance from a surface perspective. *Climate Dynamics*, **40**, 3107-3134.

910   Williams, R. G., V. Roussenov, M. S. Lozier and D. Smith, 2015: Mechanisms of heat

911 content and thermocline change in the subtropical and subpolar North Atlantic. *J. Climate*, **28**,

912 9803-9815, doi: 10.1175/JCLI-D-15-0097.1

913   Xie, S.-P., Y. Kosaka, and Y.M. Okumura, 2016: Distinct energy budgets for

914 anthropogenic and natural changes during global warming hiatus. *Nature Geoscience*, **9**, 29-

915 33.

916

	HadCM3 control simulation	Wild et al. (2013) observation based estimates
TOA incident solar	341.4	340 (340-341)
TOA outgoing solar	101.1	100 (96-100)
Atmospheric solar absorption	76.1	79 (74-91)
Surface incident solar	188.5	185 (179-189)
Surface reflected solar	24.3	24 (22-26)
Surface solar absorption	164.2	161 (154-166)
Outgoing longwave	240.5	239 (236-242)
Surface upwelling longwave	394.6	398 (394-400)
Surface downwelling longwave	332.0	342 (338-348)
Surface sensible heat	17.0	20 (15-25)
Surface latent heat	84.1	84 (70-85)

917

918   Table 1. Summary of annual mean energy flows (W m^{-2}) in the Hadcm3 control

919 simulation and comparison with observational estimates) Note that, as defined by Wild et al.

920   (2013), the TOA outgoing solar comprises all reflected solar radiation including that reflected

921   from the surface.

922

923   **Figure Captions**

924   Fig. 1. Derivation of the watermass transformation equations (a) Volume conservation

925   for waters with potential temperature less than or equal to θ (b) Heat conservation for the

926   same region (c) watermass formation rate between isopycnals θ and $\theta + \delta\theta$ due to surface

927   flux forcing. Illustration of 3D watermass transformation diagnostics (d) ocean temperature in

928   the western tropical Pacific (contours). Surface waters below 22°C are shaded brown. Surface

929   and subsurface waters with temperatures between 22°C and 23°C are shaded purple. Coloured

930   arrows indicate watermass transformation by air-sea heat exchange (yellow) and ocean

931   circulation/overturning (green) across the 22°C and 23°C isotherms. Solid (dashed) black

932   arrows indicated diapycnal mixing across the 23°C (22°C) isotherm (e) as (d) but for a

933   domain extended slightly to the south. The corresponding diapycnal mixing in the southward

934   extension to the domain is indicated by hollow arrows.

935

936   Fig. 2. Time series of ensemble mean global mean area-weighted temperature

937   anomaly (K) with respect to the 140-year control. Annual means are plotted and a 4-year

938   boxcar filter is applied to smooth the data. Colour shading indicates values significantly

939   different from the control simulation at the 95% confidence level. The dotted vertical line

940   separates the hiatus period (years 1-10, doubled vertical diffusivity) from the surge period

941   (years 11-20, standard vertical diffusivity).

942

943   Fig. 3. Ensemble mean zonal mean temperature anomaly (K) with respect to the 140–

944   year control mean during (a) hiatus period (years 6–10) (b) surge period (years 11-15). Thick

945   black contour denotes values significantly different from the control simulation at the 95%

946   confidence level. Thin black contours denote the control mean temperature (°C).

947

948   Fig. 4. Ensemble mean SST minus 140-year mean control SST (K) during (a) hiatus

949   period (years 6–10) (b) surge period (years 11–15) (c) and (d) as (a) and (b) for 0–1000m

950   heat content (TJ) (e) and (f) as (a) and (b) for net surface heat flux (W m^{-2}). Heat flux is

951   positive downward. Thin black contour line denotes values that are significantly different

952   from the control simulation at the 95% confidence level.

953

954   Fig. 5. Ensemble annual mean anomalous global energy flows (W m^{-2}) (a) Short wave

955   terms. Black – TOA upwards shortwave; red – atmospheric shortwave absorption; green

956   incident surface shortwave; blue – reflected shortwave; cyan – oceanic shortwave absorption

957   (b) Long wave and turbulent heat flux terms. Black – Outgoing Longwave Radiation at TOA;

958   red – surface upwelling longwave radation; green – incident downwelling longwave radiation;

959   blue – sensible heat flux; cyan – latent heat flux. Coloured horizontal lines denote zero

960   anomaly. In order to allow the individual anomalies to be seen clearly, each quantity has had

961   an offset subtracted – black – no offset, red –1 W m^{-2}, Green –2.5 W m^{-2}; blue –3 W m^{-2};

962   cyan –4 W m^{-2}. Annual means are plotted and a 4-year boxcar filter is applied to smooth the

963   data. Thick portions of the curves indicate values significantly different from the control

964   simulation at the 95% confidence level. The dotted vertical line separates the hiatus period

965   (years 1–10, doubled vertical diffusivity) from the surge period (years 11–20 standard vertical

966   diffusivity).

967

968   Fig. 6. Ensemble mean global annual mean net ocean heat uptake (net ocean surface

969   downward heat flux) (W m^{-2}) is indicated by the thick red line. Thin red lines indicate ±1

41

970   ensemble standard deviation. Annual means are plotted and a 4-year boxcar filter is applied to

971   smooth the data. The vertical black line is centered on the 140-year mean value from the

972   control simulation and indicates ±1 standard deviations (or ±2 standard errors). The dotted

973   vertical line separates the hiatus period (years 1–10, doubled vertical diffusivity) from the

974   surge period (years 11–15, standard vertical diffusivity).

975

976   Fig. 7. Ensemble mean global mean SST (°C) is indicated by the thick red line. Thin

977   red lines indicate ±1 ensemble standard deviation. The green line shows global mean SST for

978   an individual ensemble member run out for 50 years. Monthly means are plotted and a 36-

979   month boxcar filter is applied to smooth the data. The vertical black line is centered on the

980   140-year mean value from the control simulation and indicates ±1 standard deviations (or ±2

981   standard errors). The dotted vertical line separates the hiatus period (years 1–10, doubled

982   vertical diffusivity) from the surge period (years 11–20, standard vertical diffusivity).

983

984   Fig. 8. Scatter plot of global annual mean SAT versus SST (both in °C) for control

985   (red circles), hiatus period (years 1–10 of the ensemble experiment, black symbols) and surge

986   period (years 11–20 of the ensemble experiment, blue symbols). Individual ensemble

987   members are differentiated by different symbols: circles, stars, squares and triangles.

988

989   Fig. 9. Transformation streamfunctions (Sv) for the 140-year control simulation in

990   temperature space (a) time derivative (b) ocean circulation (c) surface heat flux (d) mixing.

991   Blue (red) shading and arrows indicate clockwise (anticlockwise) transformation. Black lines

992   show the average SST at each latitude and ±1 standard deviation.

993

994   Fig. 10. (a) Latitudinal divergence of the volume flux (Sv/°latitude) across isopycnals

995   (transformation rate) at the Equator (3°S–3°N) as a function of temperature associated with

996   surface heat flux (green), overturning (red), mixing (blue). Green circles demarcate the

997   boundaries between the prevailing thermal regimes. (b) as (a) for the "subtropical" regions

998   (average of 18°S–12°S and 12°N–18°N).

999

1000   Fig. 11. (a) Formation rate (Sv/°latitude) at the Equator (3°S–3°N) in the control

1001   simulation associated with overturning (red), surface heat flux (green), mixing (blue) for the

1002   four thermal regimes (i–iv) defined in Fig. 8. (b) as (a) for the "subtropical" regions (average

1003   of 18°S–12°S and 12°N–18°N).

1004

1005   Fig. 12. Logarithm to base ten of the ratio of ensemble mean to control seawater

1006   volume in temperature classes (1K bins centered on integral values). Evaluated over the

1007   global ocean. The dotted vertical line separates the hiatus period (years 1–10, doubled vertical

1008   diffusivity) from the surge period (years 11–15, standard vertical diffusivity).

1009

1010   Fig. 13. (a) Logarithm to base ten of the control simulation seawater volume in

1011   temperature classes (1K bins centered on integral values) evaluated at each latitude. (b)

1012   Logarithm to base ten of the ratio of ensemble mean to control global seawater volume in

1013   temperature classes (1K bins centered on integral values). Blue – average over hiatus period;

1014   red – average over surge period. Vertical black line indicates a zero value. (c) Logarithm to

1015   base ten of the ratio of ensemble mean to control seawater volume in temperature classes (1K

1016   bins centered on integral values). Evaluated at each latitude and averaged over the hiatus

1017   period, years 1–10 (d) as (c) for the surge period, years 11–20. Black lines show the average

1018   SST at each latitude and ±1 standard deviation.

1019

1020   Fig. 14. Ensemble mean anomalous formation rate (Sv/°latitude) at the Equator (3°S–

1021   3°N) associated with overturning (red), surface heat flux (green), mixing (blue) and volume

1022   change (cyan) for the four thermodynamic regimes (i–iv) defined in Fig. 8. (a) years 1–5 (b)

1023   year 6–10 (c) years 11–15 (d) years 16–20. (e)–(h) as (a)–(d) for the "subtropical" regions

1024   (average of 18°S–12°S and 12°N–18°N).

1025

1026   Fig 15 (a) Ensemble mean anomalous overturning streamfunction (Sv) in the

1027   subtropics (colour shading) for years 1–5 (b) year 6–10 (c) years 11–15 (d) years 16–20 (e)

1028   ensemble mean anomalous zonal wind (m s^{-1}) for years 1-5 (f) year 6–10 (g) years 11–15 (h)

1029   years 16–20. Thick black contour and dotted regions denote anomalies significantly different

1030   from the control simulation at the 95% confidence level. Thin black contours in (a)-(d) denote

1031   the control mean streamfunction (Sv).

1032

1033   Fig. 16. (a) Temperature anomaly (K) predicted by the conceptual model. The dotted

1034   vertical line separates the hiatus period (years 121–130, higher vertical diffusivity) from the

1035   surge period (years 131–160, standard vertical diffusivity). (b) anomaly-depth profile

1036   predicted by the conceptual model at hiatus year 125 (red); surge year 145 (cyan). (c)

1037   Ensemble mean zonally averaged Equatorial (3°S–3°N) temperature anomaly profile from the

1038   coupled climate model experiment as a function of depth in the Pacific Ocean averaged over

1039   the hiatus period (red); first year of the surge (cyan); (d) as (c) except for the off-equatorial

1040   regions (average of 18°S–12°S and 12°N–18°N). Cyan line shows average over year 3 of the

1041   surge.

1042

1043   Fig. 17. Schematic of the hiatus to surge mechanism described in this paper (a)

1044   conditions during hiatus (b) conditions during surge (c) conditions after surge.

1045

1046

Fig. 1. Derivation of the watermass transformation equations (a) Volume conservation for waters with potential temperature les than or equal to theta (b) Heat conservation for the same region (c) watermass formation rate between isopycnals θ and $\theta + \delta\theta$ due to surface flux forcing. Illustration of 3D watermass transformation diagnostics (d) ocean temperature in the western tropical Pacific (contours). Surface waters below 22°C are shaded brown. Surface and subsurface waters with temperatures between 22°C and 23°C are shaded purple. Coloured arrows indicate watermass transformation by air-sea heat exchange (yellow) and ocean circulation/overturning (green) across the 22°C and 23°C isotherms. Solid (dashed) black arrows indicated diapycnal mixing across the 23°C (22°C) isotherm (e) as (d) but for a domain extended slightly to the south. The corresponding diapycnal mixing in the southward extension to the domain is indicated by hollow arrows.

1058

1059

46
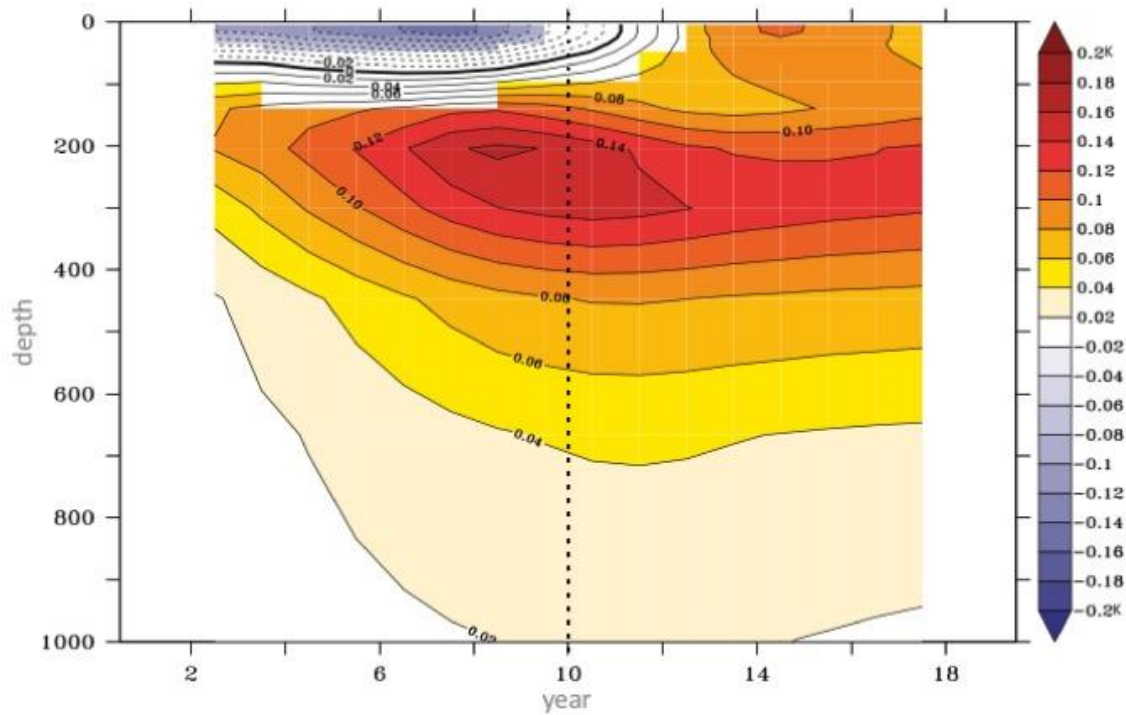
Fig. 2. Time series of ensemble mean global mean area-weighted temperature anomaly (K) with respect to the 140-year control. Annual means are plotted and a 4-year boxcar filter is applied to smooth the data. Colour shading indicates values significantly different from the control simulation at the 95% confidence level. The dotted vertical line separates the hiatus period (years 1-10, doubled vertical diffusivity) from the surge period (years 11-20, standard vertical diffusivity).
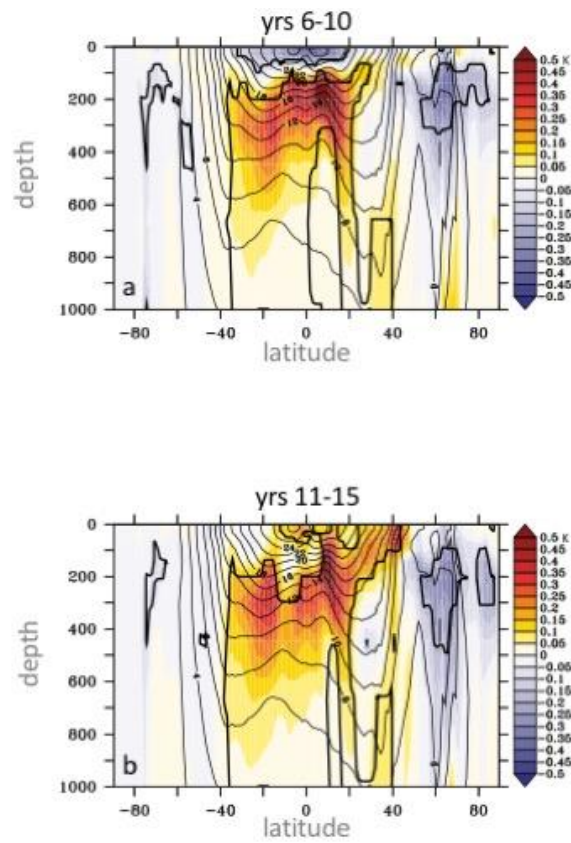
Fig. 3. Ensemble mean zonal mean temperature anomaly (K) with respect to the 140–year control mean during (a) hiatus period (years 6–10) (b) surge period (years 11-15). Thick black contour denotes values significantly different from the control simulation at the 95% confidence level. Thin black contours denote the control mean temperature (°C).
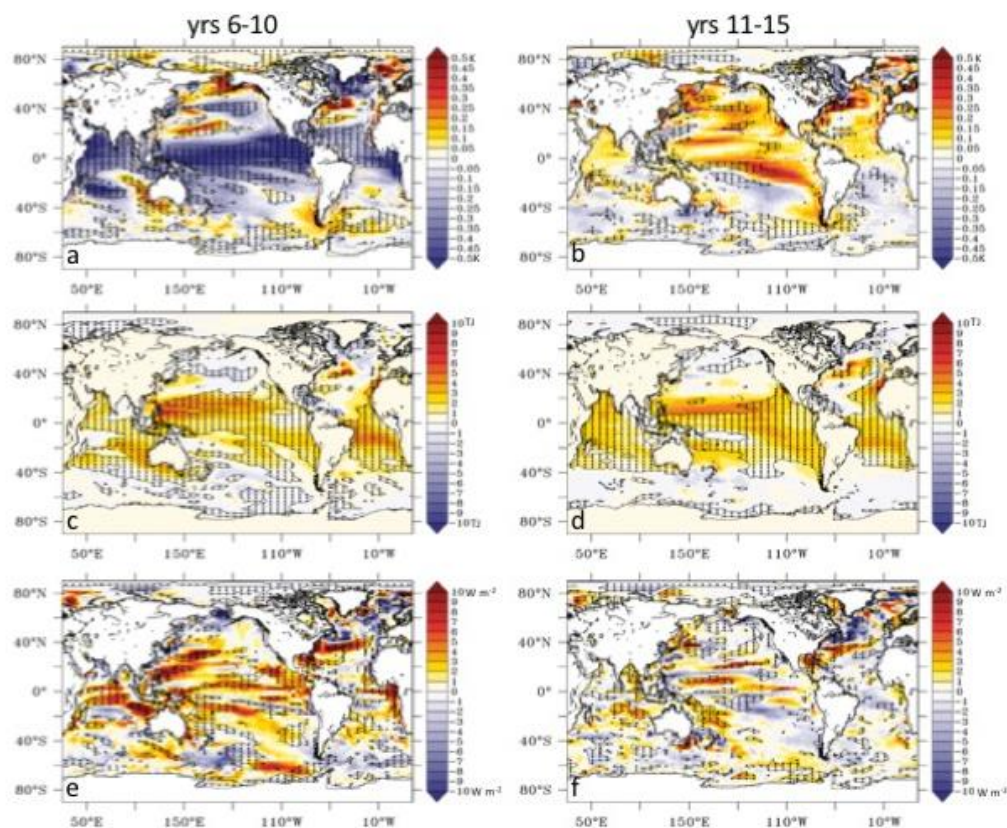
Fig. 4. Ensemble mean SST minus 140-year mean control SST (K) during (a) hiatus period (years 6–10) (b) surge period (years 11–15) (c) and (d) as (a) and (b) for 0–1000m heat content (TJ) (e) and (f) as (a) and (b) for net surface heat flux (W m^{-2}). Heat flux is positive downward. Thin black contour line denotes values that are significantly different from the control simulation at the 95% confidence level.
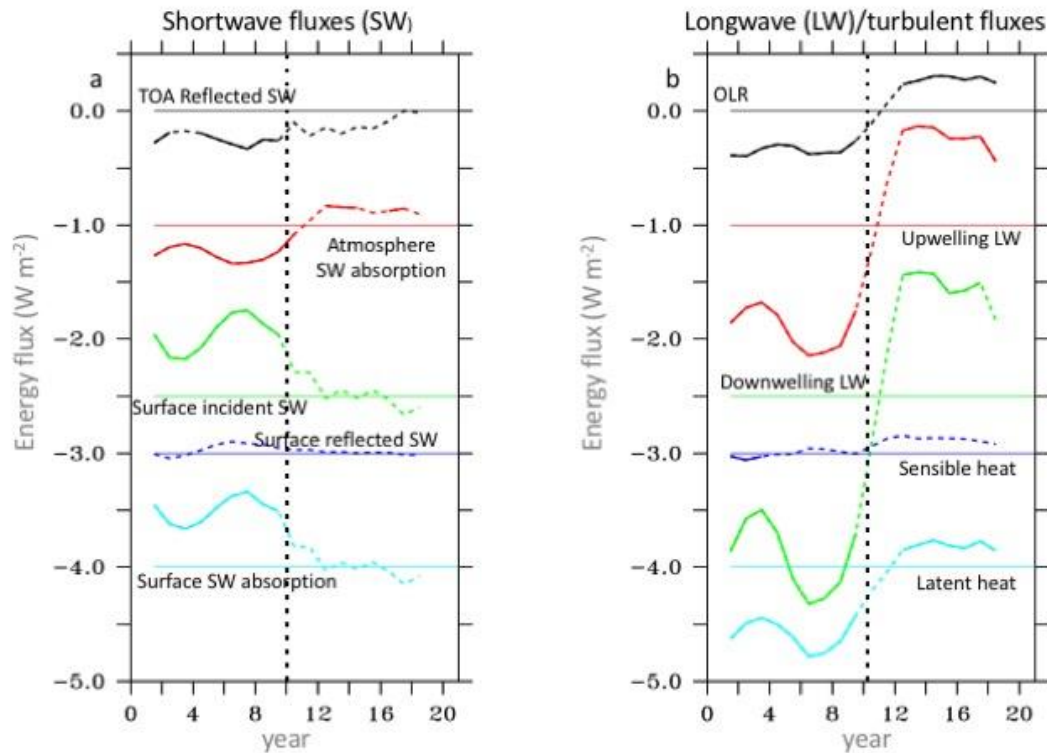
Fig. 5. Ensemble annual mean anomalous global energy flows (W m^{-2}) (a) Short wave terms. Black – TOA upwards shortwave; red – atmospheric shortwave absorption; green incident surface shortwave; blue – reflected shortwave; cyan – oceanic shortwave absorption (b) Long wave and turbulent heat flux terms. Black – Outgoing Longwave Radiation at TOA; red – surface upwelling longwave radation; green – incident downwelling longwave radiation; blue – sensible heat flux; cyan – latent heat flux. Coloured horizontal lines denote zero anomaly. In order to allow the individual anomalies to be seen clearly, each quantity has had an offset subtracted – black – no offset, red –1 W m^{-2}, Green –2.5 W m^{-2}; blue –3 W m^{-2}; cyan –4 W m^{-2}. Annual means are plotted and a 4-year boxcar filter is applied to smooth the data. Thick portions of the curves indicate values significantly different from the control simulation at the 95% confidence level. The dotted vertical line separates the hiatus period (years 1–10, doubled vertical diffusivity) from the surge period (years 11–20 standard vertical diffusivity).
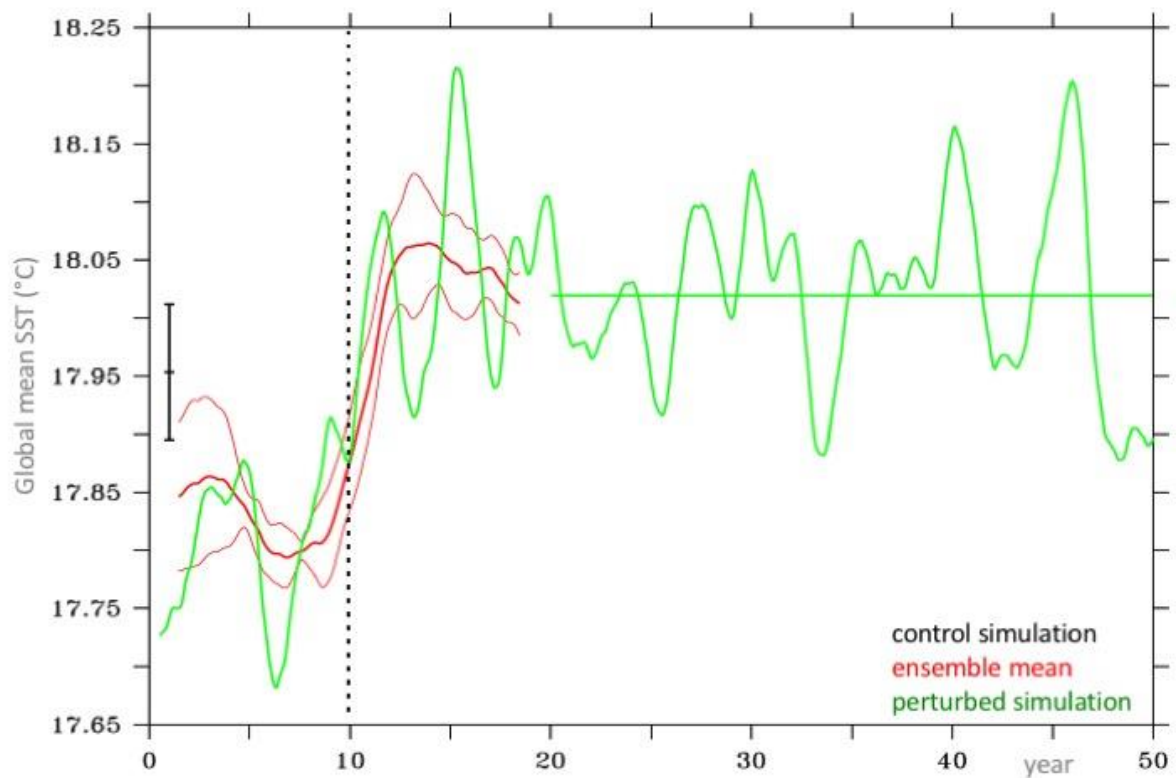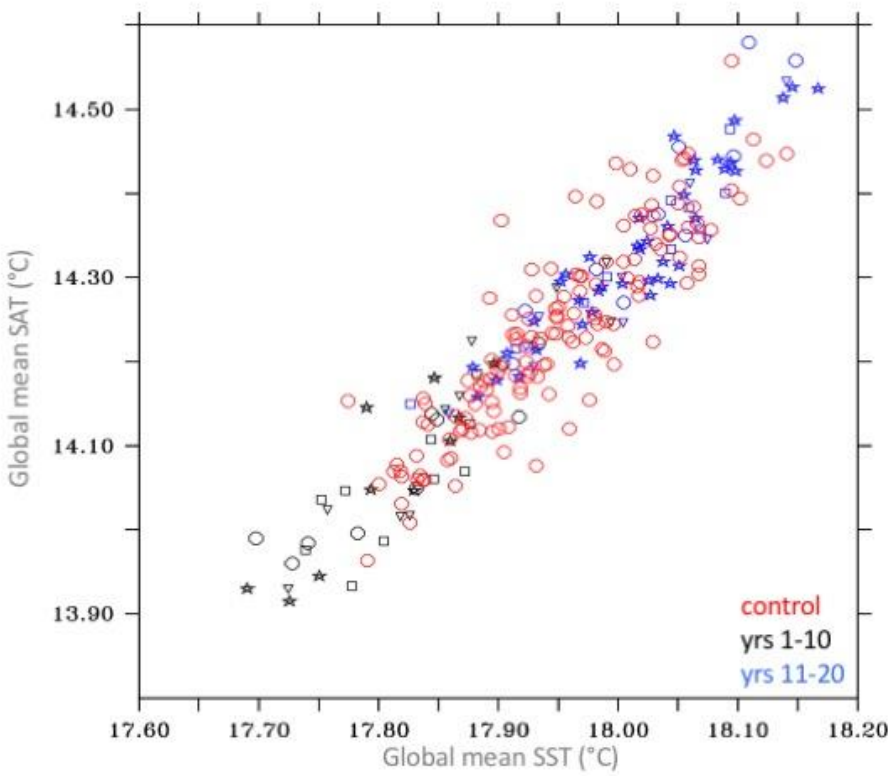
1125

1126

1127

1128

1129

1130

1131

1132

1133

1134

1135   Fig. 6. Ensemble mean global annual mean net ocean heat uptake (net ocean surface

1136   downward heat flux) (W m^{-2}) is indicated by the thick red line. Thin red lines indicate ±1

1137   ensemble standard deviation. Annual means are plotted and a 4-year boxcar filter is applied to

1138   smooth the data. The vertical black line is centered on the 140-year mean value from the

1139   control simulation and indicates ±1 standard deviations (or ±2 standard errors). The dotted

1140   vertical line separates the hiatus period (years 1–10, doubled vertical diffusivity) from the

1141   surge period (years 11–15, standard vertical diffusivity).

1142

1143
1144

1145

1146

1147   Fig. 7. Ensemble mean global mean SST (°C) is indicated by the thick red line. Thin

1148   red lines indicate ±1 ensemble standard deviation. The green line shows global mean SST for

1149   an individual ensemble member run out for 50 years. Monthly means are plotted and a 36-

1150   month boxcar filter is applied to smooth the data. The vertical black line is centered on the

1151   140-year mean value from the control simulation and indicates ±1 standard deviations (or ±2

1152   standard errors). The dotted vertical line separates the hiatus period (years 1−10, doubled

1153   vertical diffusivity) from the surge period (years 11−20, standard vertical diffusivity).

1154
1155
1156
1157
1158
1159

1160

1161
1162
1163
1164
1165
1166   Fig. 8. Scatter plot of global annual mean SAT versus SST (both in °C) for control

1167   (red circles), hiatus period (years 1–10 of the ensemble experiment, black symbols) and surge

1168   period (years 11–20 of the ensemble experiment, blue symbols). Individual ensemble

1169   members are differentiated by different symbols: circles, stars, squares and triangles.
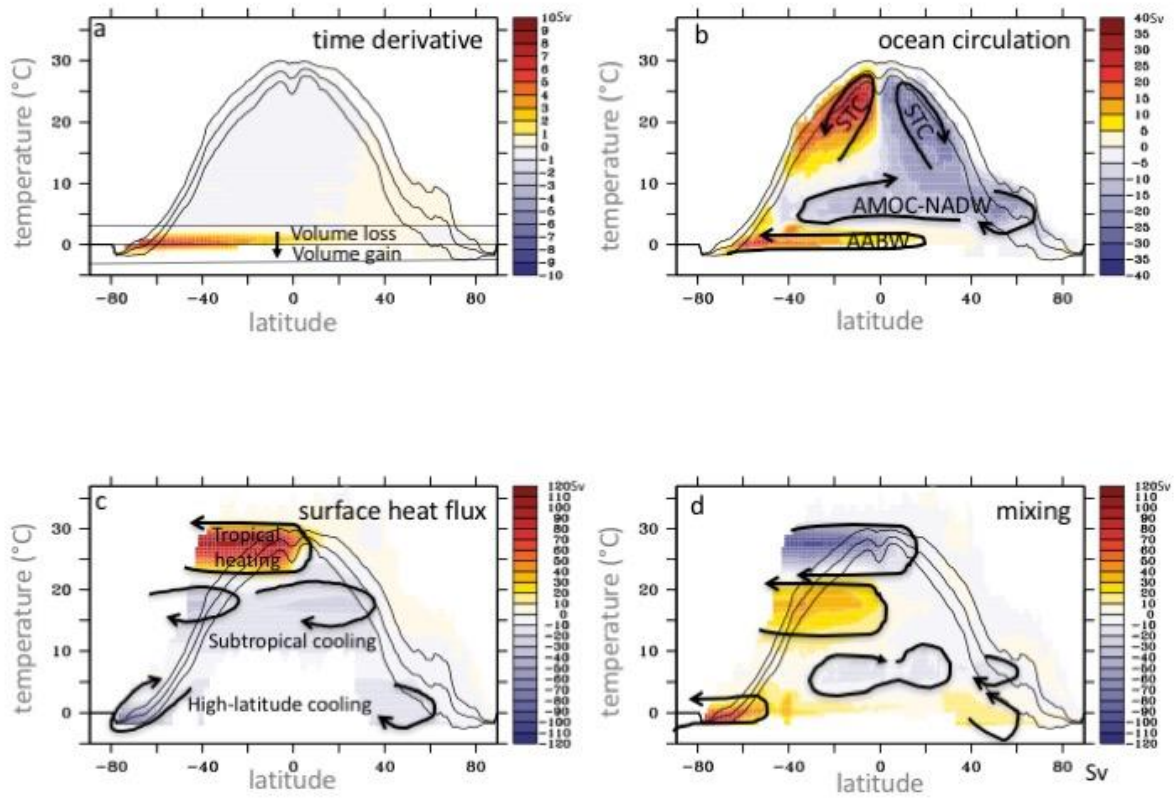
1170
1171
1172
1173
1174
1175
1176

1177

1178   Fig. 9. Transformation streamfunctions (Sv) for the 140-year control simulation in

1179   temperature space (a) time derivative (b) ocean circulation (c) surface heat flux (d) mixing.

1180   Blue (red) shading and arrows indicate clockwise (anticlockwise) transformation. Black lines

1181   show the average SST at each latitude and ±1 standard deviation.

1182
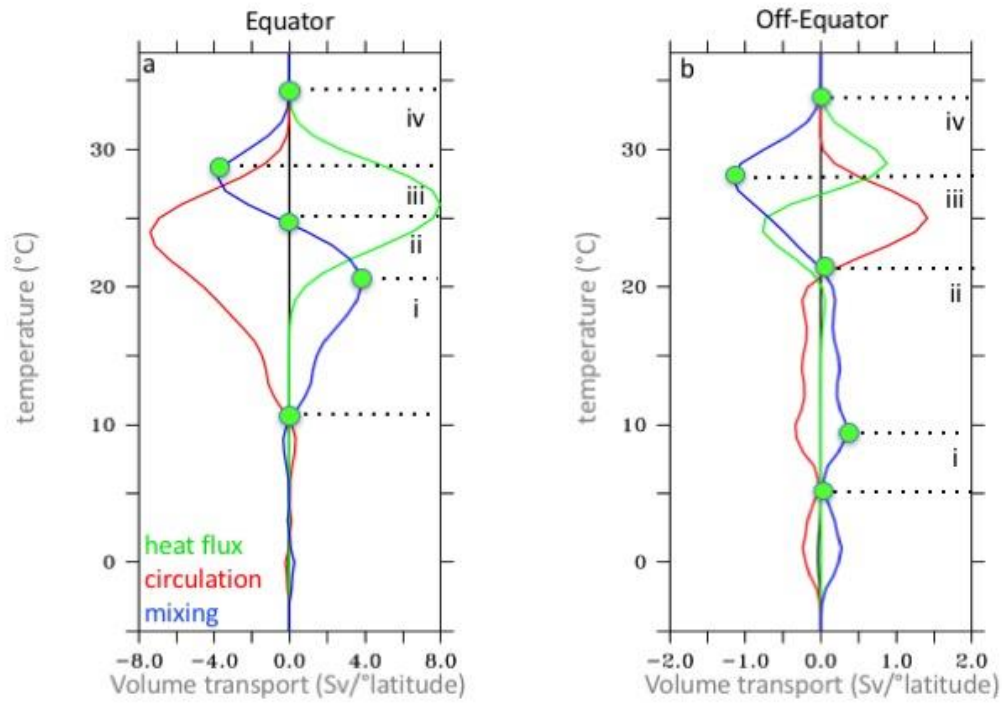
Fig. 10. (a) Latitudinal divergence of the volume flux (Sv/°latitude) across isopycnals (transformation rate) at the Equator (3°S–3°N) as a function of temperature associated with surface heat flux (green), overturning (red), mixing (blue). Green circles demarcate the boundaries between the prevailing thermal regimes. (b) as (a) for the "subtropical" regions (average of 18°S–12°S and 12°N–18°N).
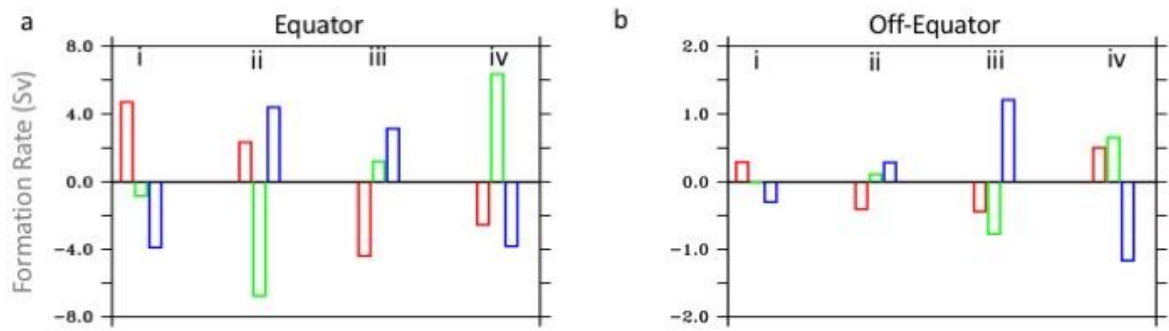
Fig. 11. (a) Formation rate (Sv/°latitude) at the Equator (3°S–3°N) in the control simulation associated with overturning (red), surface heat flux (green), mixing (blue) for the four thermal regimes (i–iv) defined in Fig. 8. (b) as (a) for the "subtropical" regions (average of 18°S–12°S and 12°N–18°N).
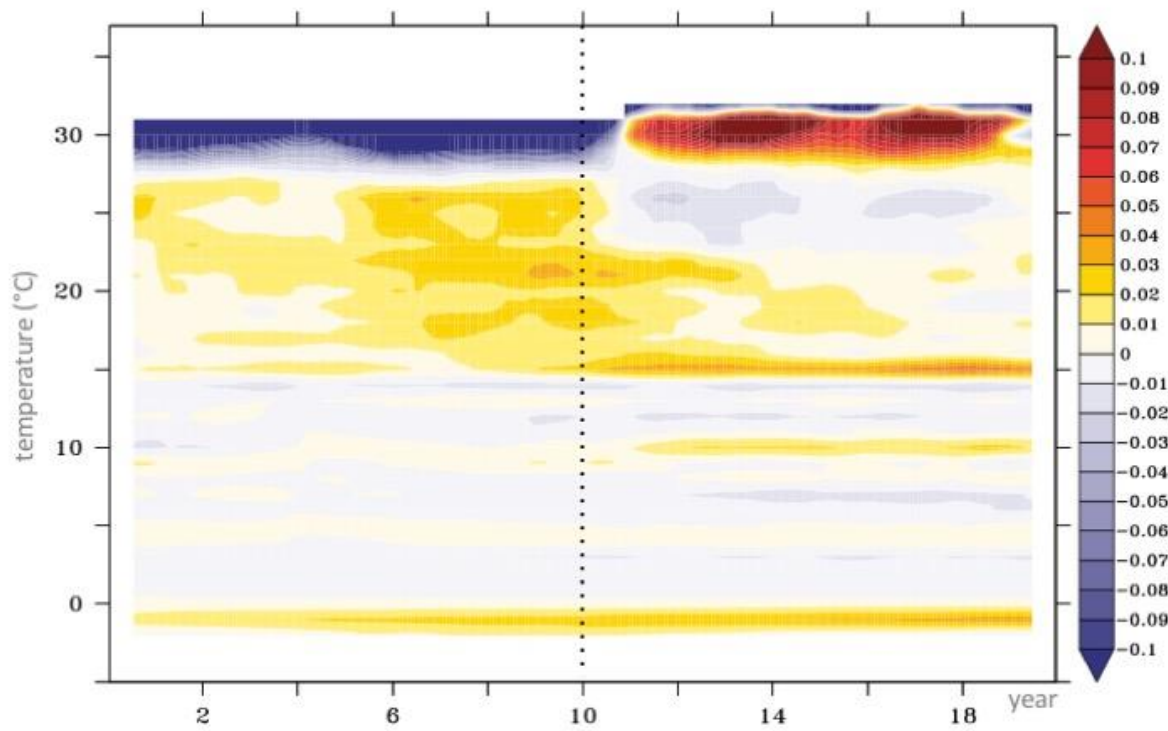
1199

1200

Fig. 12. Logarithm to base ten of the ratio of ensemble mean to control seawater volume in temperature classes (1K bins centered on integral values). Evaluated over the global ocean. The dotted vertical line separates the hiatus period (years 1–10, doubled vertical diffusivity) from the surge period (years 11–15, standard vertical diffusivity).
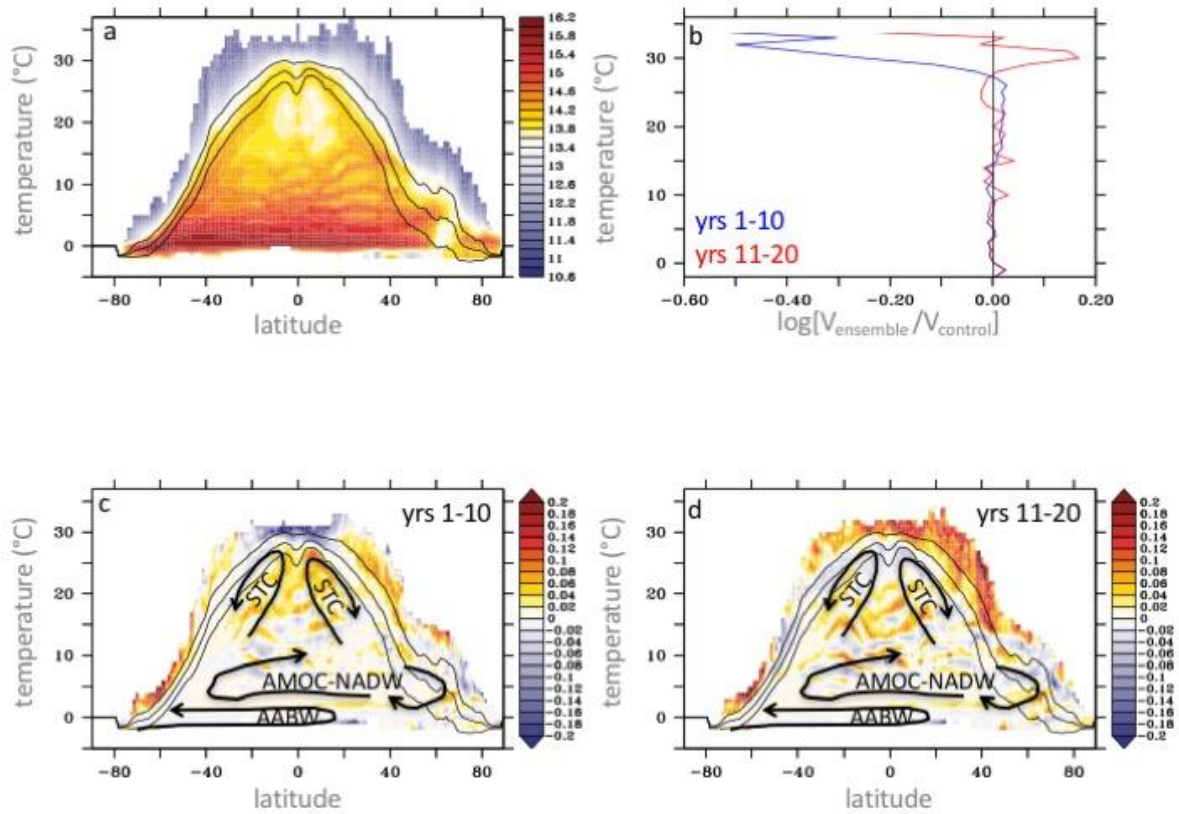
1201

1202

1203

1204

1205

1206

1207

1208   Fig. 13. (a) Logarithm to base ten of the control simulation seawater volume in

1209   temperature classes (1K bins centered on integral values) evaluated at each latitude. (b)

1210   Logarithm to base ten of the ratio of ensemble mean to control global seawater volume in

1211   temperature classes (1K bins centered on integral values). Blue – average over hiatus period;

1212   red – average over surge period. Vertical black line indicates a zero value. (c) Logarithm to

1213   base ten of the ratio of ensemble mean to control seawater volume in temperature classes (1K

1214   bins centered on integral values). Evaluated at each latitude and averaged over the hiatus

1215   period, years 1–10 (d) as (c) for the surge period, years 11–20. Black lines show the average
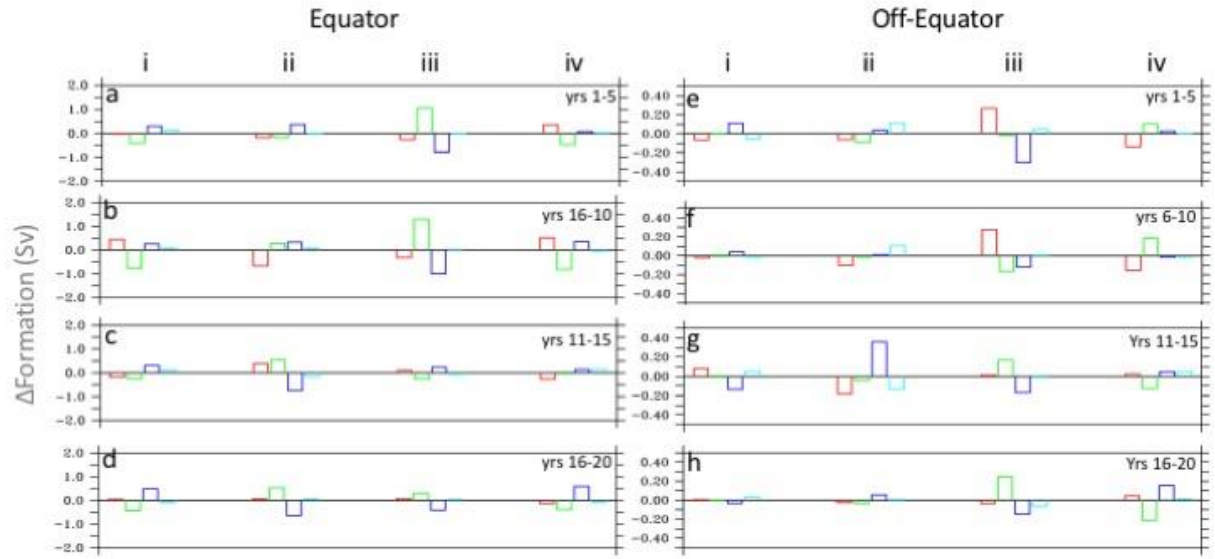
1216   SST at each latitude and ±1 standard deviation.

1217
1218

1219

1220

Fig. 14. Ensemble mean anomalous formation rate (Sv/°latitude) at the Equator (3°S–3°N) associated with overturning (red), surface heat flux (green), mixing (blue) and volume change (cyan) for the four thermodynamic regimes (i–iv) defined in Fig. 8. (a) years 1–5 (b) year 6–10 (c) years 11–15 (d) years 16–20. (e)–(h) as (a)–(d) for the "subtropical" regions (average of 18°S–12°S and 12°N–18°N).
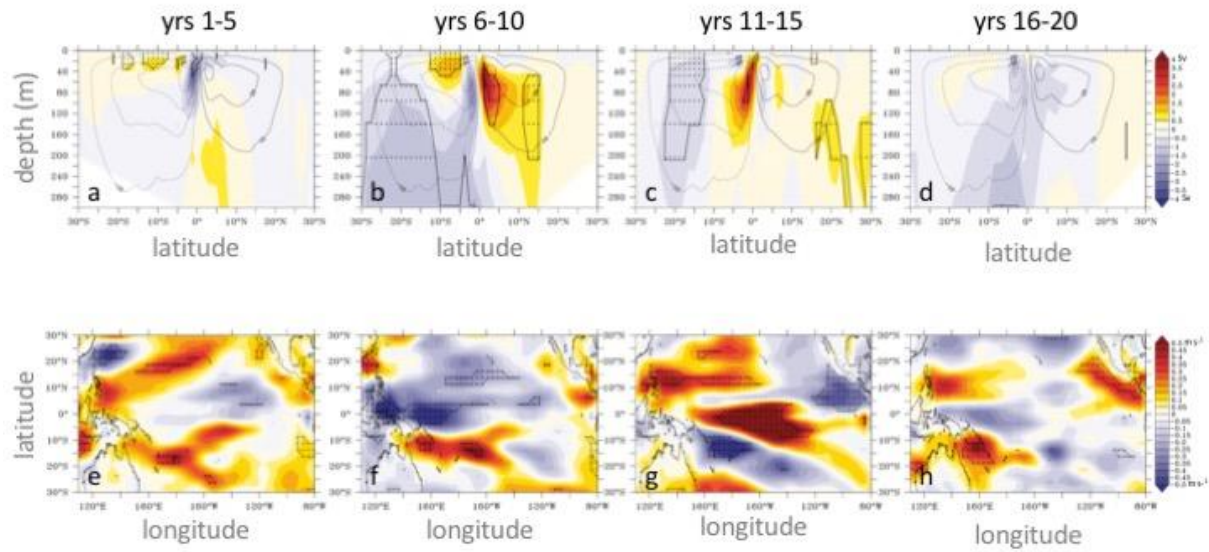
Fig 15 (a) Ensemble mean anomalous overturning streamfunction (Sv) in the

subtropics (colour shading) for years 1–5 (b) year 6–10 (c) years 11–15 (d) years 16–20 (e)

ensemble mean anomalous zonal wind (m s^{-1}) for years 1-5 (f) year 6–10 (g) years 11–15 (h)

years 16–20. Thick black contour and dotted regions denote anomalies significantly different

from the control simulation at the 95% confidence level. Thin black contours in (a)-(d) denote

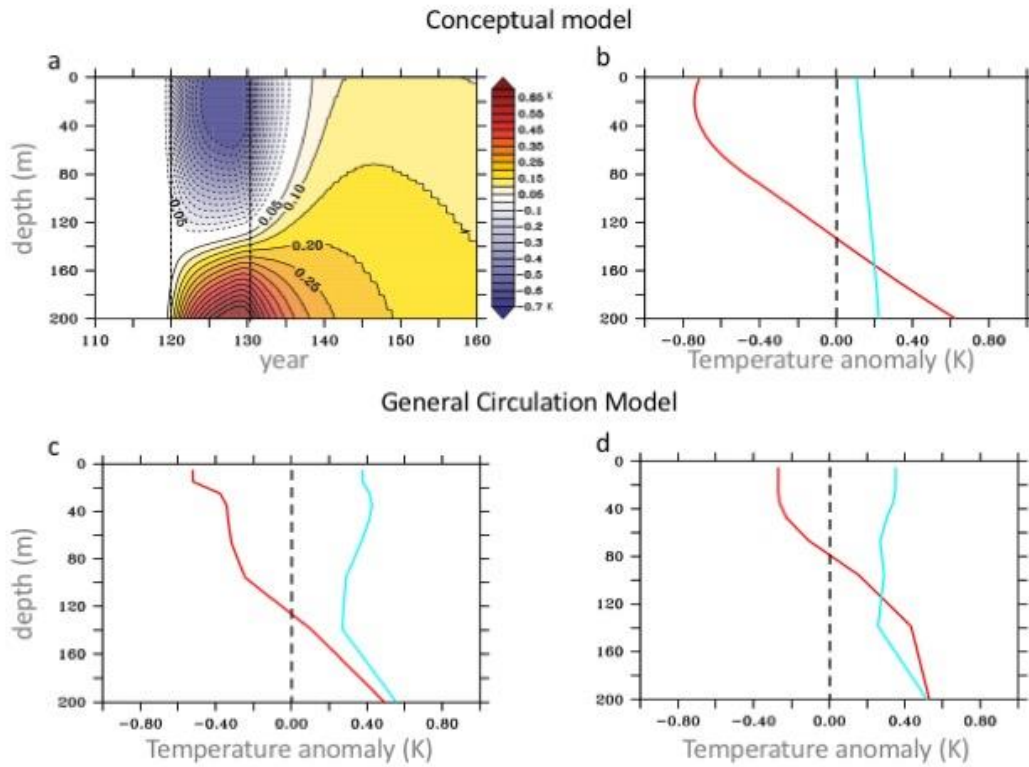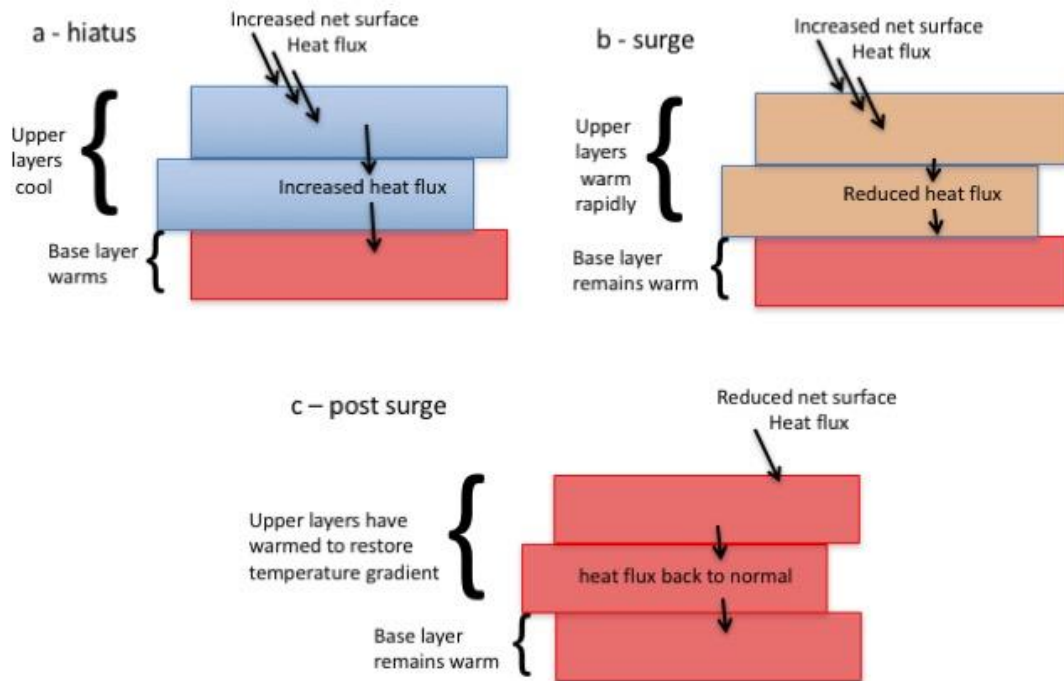the control mean streamfunction (Sv).

Fig. 16. (a) Temperature anomaly (K) predicted by the conceptual model. The dotted vertical line separates the hiatus period (years 121–130, higher vertical diffusivity) from the surge period (years 131–160, standard vertical diffusivity). (b) anomaly-depth profile predicted by the conceptual model at hiatus year 125 (red); surge year 145 (cyan). (c) Ensemble mean zonally averaged Equatorial (3°S–3°N) temperature anomaly profile from the coupled climate model experiment as a function of depth in the Pacific Ocean averaged over the hiatus period (red); first year of the surge (cyan); (d) as (c) except for the off-equatorial regions (average of 18°S–12°S and 12°N–18°N). Cyan line shows average over year 3 of the surge.

61

Hiatus to surge mechanism

a - hiatus

Increased net surface Heat flux

Upper layers cool

Increased heat flux

Base layer warms

b - surge

Increased net surface Heat flux

Upper layers warm rapidly

Reduced heat flux

Base layer remains warm

c – post surge

Reduced net surface Heat flux

Upper layers have warmed to restore temperature gradient

heat flux back to normal

Base layer remains warm

1259

1260

1261   Fig. 17. Schematic of the hiatus to surge mechanism described in this paper (a)

1262   conditions during hiatus (b) conditions during surge (c) conditions after surge.